Corrosion Behaviour of Materials in H_2S Abatement System for Geothermal Power Plants

Sölvi Már Hjaltason

CORROSION BEHAVIOUR OF MATERIALS IN H$_2$S ABATEMENT SYSTEM FOR GEOTHERMAL POWER PLANTS

Sölvi Már Hjaltason

60 ECTS thesis submitted in partial fulfillment of a
Magister Scientiarum degree in Mechanical Engineering

Advisor
Sigrún Nanna Karlsdóttir
Kolbrún Ragna Ragnarsdóttir

External Examiner
Geir Þórólfsson

Faculty of Industrial Engineering,
Mechanical Engineering and Computer Science
School of Engineering and Natural Sciences
University of Iceland
Reykjavik, October 2015

Corrosion Behaviour of Materials in H_2S Abatement System for Geothermal Power Plants
Corrosion experiments in H_2S abatement
60 ECTS thesis submitted in partial fulfillment of a M.Sc. degree in Mechanical Engineering

Faculty of Industrial Engineering,
Mechanical Engineering and Computer Science
School of Engineering and Natural Sciences
University of Iceland
Hjarðarhagi 6
107, Reykjavik, Reykjavik
Iceland

Telephone: 525 4000

To my family

Abstract

Geothermal energy is a sustainable and clean energy source. Among renewable energy sources geothermal energy is environmentally attractive since the resource can be utilized continuously and is not dependent on weather conditions. When utilized, however, gases such as carbon dioxide (CO_2) and hydrogen sulfide (H_2S) are emitted to the atmosphere, these emissions are considered to be one of the main environmental, safety and health concerns of geothermal utilization. Recently Icelandic power companies started re-injecting H_2S and CO_2 back into the ground in a research project called SulFix to decrease H_2S emission from Icelandic geothermal power plants. The gases are dissolved in condensate at 25°C and 5 bars in a newly constructed air cleaning station at Hellisheiði Power Plant. In this study the corrosion behaviour of various materials including the ones chosen for the absorption tower in the cleaning station are studied in the H_2S cleaning process. Corrosion experiments were done over two time periods, 4 and 12 weeks. The specimens were installed into the absorption tower where H_2S and CO_2 are dissolved in condensate. The susceptibility to stress corrosion cracking (SCC) of the austenitic stainless steels 304L, 316L was investigated and corrosion rates were calculated for the carbon steel S235, and the stainless steels 316L and SAF 2205 for the two time periods. The results show that the material selection for the absorption tower is sufficient. 316L and SAF 2205 showed no signs of corrosion damages for all experiments while 304L experienced SCC. Results for the carbon steel S235 showed that the steel was severely damaged by hydrogen induced cracking (HIC) and had a poor performance in the tower.

Útdráttur

Jarðvarmaorka er sjálfbær og hrein orka. Á meðal endurnýjanlegra orkugjafa er jarðvarmaorka aðlaðandi þar sem hægt er að nýta hana stanlaust óháð veðurskilyrðum. Samt sem áður, við nýtingu, er gösum á borð við koldíoxíð (CO_2) og brennisteinsvetni (H_2S) hleypt út í andrúmsloftið, þessi útblástursefni eru talin vera helsta ógn við umhverfi, öryggi og heilbrigði af völdum jarðvarma nýtingarinnar. Nýlega fóru íslensk orkufyrirtæki að dæla niður H_2S og CO_2 aftur ofan í jörðina í tilraunaverkefni sem kallast SulFix til þess að minnka losun H_2S frá íslenskum jarðvarmaverum. Gösin eru leyst upp í þéttivatni við 25°C og 5 bör í nýuppsettri lofthreinsistöð við Hellisheiðarvirkjun. í þessari rannsókn er tæringarhegðun nokkurra málma þar á meðal þess sem valin var fyrir lofthreinsiturn stöðvarinnar rannsökuð í H_2S hreinsunarferlinu. Tæringar tilraunir voru gerðar með tveimur tímabilum, 4 og 12 vikur. Sýnin voru sett inn í lofthreinsiturninn þar sem leysni H_2S og CO_2 á sér stað í þéttivatninu. Næmni spennutæringar (SCC) fyrir austenísku ryðfríu stálin 304L og 316L voru rannsökuð og tæringarhraðar reiknaðir fyrir svart stál S235, og ryðfríu stálin 316L og SAF 2205 fyrir bæði tímabilin. Niðurstöðurnar sýna að efnisvalið fyrir lofthreinsiturninn sé nægjanlegt. 316L og SAF 2205 sýndu engin merki um tæringu fyrir allar tilraunir á meðan 304L varð fyrir SCC. Niðurstöður fyrir svarta stálið sýndu að það var alvarlega skemmt af völdum vetnisskemmda (HIC) og hafði laka frammistöðu í turninum.

Contents

Contents

List of Figures

List of Tables

List of Abbreviations

ASTM American Society for Testing and Materials

BCC Body Centered Cubic

EIC Environmental Induced Cracking

HIC Hydrogen Induced Cracking

ppm parts per million

SCC Stress Corrosion Cracking

SEM Scanning Electron Microscope

SOHIC Stress-oriented Hydrogen Induced Cracking

SSC Sulfide Stress Corrosion

XEDS X-ray Energy Dispersive Spectroscope

Acknowledgments

1. Introduction

Geothermal energy is a sustainable and clean energy source. Among renewable energy sources geothermal energy is environmentally attractive since the resource can be utilized continuously and is not dependent on weather conditions. When utilized, however, gases such as carbon dioxide (CO_2) and hydrogen sulfide (H_2S) are emitted to the atmosphere, these emissions are considered to be one of the main environmental, safety and health concerns of geothermal utilization (Nagl, 2010).

Geothermal energy is a widely available resource and the use of geothermal energy has been growing significantly. The heat from the earth's crust is becoming an important future energy source. Compared to other generation types such as fossil fuel, geothermal energy has substantially less emissions. Matek (2014) predicts that in 2017, energy consumption could reach 13,450 MW_e and according to the prediction from Bertani (2012) countries utilizing geothermal energy would increase from 25 to 46 over a five year period from 2010 to 2015. New report from Bertani (2015) shows that on this five year period installed capacity of geothermal energy has increased of about 1,700 MW_e, thus the total energy consumption today is 12,635 MW_e where the top five countries in added MW_e in percentages (%) from 2010 are Turkey, Germany, Kenya, Nicaragua and New Zealand. Bertani (2015) also lays out a short term forecast for 2020, where geothermal energy installed capacity would reach 21,433 MW_e based on his previous work in this study and that the target for 2050 is 140,000 MW_e in total (taking into account EGS an other non conventional resources). This increase in energy consumption could make geothermal energy represent 8.3% of the worlds total electricity production, which is considered to be the total electricity production possible from geothermal energy (World Energy Council, 2013), saving up to 1,000 million tons per year of CO_2 emissions (Bertani, 2015).

Geothermal heat can be found all over the world, ranging from 20°C to over 300°C. Not all of those resources can be utilized for electricity productions since it is feasible that the resource is located on a high temperature field with reservoir temperature over 150°C. Most of high temperature fields are situated along plate boundaries, where there is volcanic activity and magma intrusions with partly molten rock at temperature above 1000°C at a few kilometers depth. The molten rock heats up the groundwater which can be used for power production. Highly fractured crust at the plate boundaries are essential for utilizing the fields since its permeability allows groundwater flow in and out of the reservoir. However, cold geothermal fields can be utilizedfor electricity production with binary cycles like the example at Chena Hot Springs in Alaska shows, using temperature at 74°C (Bertani, 2015; World Energy Council, 2013).

Iceland is located on the Mid-Atlantic Ridge. The ridge is the plate boundary between

the North American and the Eurasian tectonic plates. The plates are moving apart about 2 cm per year. As a result, Iceland is one of the most tectonically active place on earth with more than 200 volcanoes running through the volcanic zone reaching from south-west to the north-east of the country. Atleast 20 fields can be found on the volcanic zone where the temperature can reach 250°C within 1000 m depth. Iceland is therefore a prime location for geothermal energy utilization. The first electrical generation from geothermal energy in Iceland started 1969 at Bjarnarflag in the north-east of Iceland and since then there have been installed seven other geothermal power plants where six of them are successfully operating today (Ragnarsson, 2010). According to Orkuspárnefnd (2014) 28.95% of all electricity generated in Iceland comes from geothermal and 71% comes from hydro power plants, the rest from wind- and fossil fuel generators.

Newest geothermal power plant in Iceland is approximately 20-30 km to the east of the capital city Reykjavík. Hellisheiði power plant is one of the largest geothermal power plants in the world and is capable of producing 303 MW_e and 133 MW_{th}. The annual emission for 2012 was around 43200 and 16900 tons of CO_2 and H_2S (Gunnarsson & Aradóttir, 2013). Hellisheiði power plant and the nearby Nesjavellir power plant are considered to be the main sources of H_2S pollution in south-west Iceland. Since Hellisheiði power plant started operating in 2006 people have noticed an increase in H_2S concentration in the capital area, both by increased corrosion in metals as well as odor nuisance, where low concentration of H_2S has the smell of "rotten eggs". H_2S pollution in Reykjavík has been studied using data from 2007 to 2009. The conclusion was that about 80 times per year H_2S concentration is over 50 μgm^{-3} for 2 hours on average, mostly occurring at night during limited range of weather conditions (Thorsteinsson et al., 2013). Another study confirmed the H_2S pollution from previous investigation. That study dramatically lowers the previous investigation by reporting that 2-6 times per year weather conditions are favourable for high H_2S concentration in Reykjavík (Olafsdottir & Gardarsson, 2013).

New legislation was set 1st of June 2010 in Iceland nr. 514/2010, the legislation set a limit to the concentration of H_2S emissions into the atmosphere. Due to the legislation power companies using geothermal energy made a mutual agreement on collaboration to construct ways to reduce the H_2S emissions from Hellisheiði power plant before 1st of July 2014. Collaboration between these energy companies led to a project called the SulFix project where the main focus is to reduce these air pollutant emissions in an economic, efficient and environmental ways ("Verkefnisáætlun SulFix: Um förgun brennisteinsvetnis frá jarðgufuvirkjunum", 2013). Part of the SulFix project is the newly constructed air cleaning station located at Hellisheiði power plant. The new air cleaning station is the second station built at Hellisheiði. Former air cleaning station was a test station which had some problems with severe scaling and corrosion of carbon steels in a distillation column and lasted for only two months (Gunnarsson et al., 2015). Also, on several occasions problems have encountered with the pipes around the abatement system which are made out of stainless steel 316L. The pipes have shown leakage in or near the welding area of the pipes and it is believed that the sour liquid with dissolved gases was able to sit at low points and initiate the corrosion, this was especially seen if the gases contained traces of oxygen. These leakages were believed to form because of bad welds but have not been verified (Arnarson, 2015).

Geothermal steam and water contains dissolved gases such as hydrogen sulfide (H_2S) and carbon dioxide (CO_2), it is commonly known that these gases are corrosive substances (Banaś et al., 2007; Kane & Cayard, 1998). These gases can cause corrosion failure in geothermal equipment and wells (Karlsdóttir, 2012). Thus, correct material selection and fabrication in equipment and pipes in direct contact with geothermal fluid and steam is very important for safe operation and decreased operating costs. A poorly selected material can for example reduce safety and increase cost due to maintenance. It should be noted that corrosion in geothermal equipment depends on factors such as the flow rate, temperature, the pressure and the pH level of the liquid that the gases are dissolved in (Conover et al., 1980; Kaya & HoShan, 2005). H_2S along with CO_2 can cause several types of corrosion, such as, general and localized corrosion, hydrogen induced cracking (HIC), stress corrosoion cracking (SCC) and sulfide stress cracking (SSC) (Karlsdóttir, 2012; Lichti, 2007).

Due to stricter legislation of gas emissions in the atmosphere in Iceland, information from this project are very valuable for construction and operation of future air cleaning stations needed to be built. Information regarding 316L performance are also extremely important for safe operation at the current air cleaning station in Hellisheiði power plant.

The Objective of this thesis is to investigate the corrosion behaviour of stainless steel 316L in the new air cleaning stations absorption tower at Hellisheiði power plant in Iceland. For comparison carbon steel S235, austenitic stainless steel 304L and a higher alloyed duplex stainless steel 2205 were tested. Corrosion experiments were carried out in the absorption tower that separates the gases and dissolves H_2S and CO_2 in geothermal condensate.

This hypothesis of this thesis is to answer the following questions. How is the performance of the 316L in the H_2S abatement process environment and how are the higher and lower grade material performing compared to the 316L. Theoretically 316L is a sufficient material for this environment. However, it has never been proven.

From this work valuable information are provided that will aid in the development of H_2S abatement systems technology which is taking place in Iceland due to stricter laws on emission of green house gases into the atmosphere. Main contributions are listed here below.

1. Introduction

- Corrosion rate for austenitic stainless steel 316L was calculated along with rates for carbon steel S235 and duplex stainless steel 2205 which can be considered to be a next step up in material selection.

- U-bent samples will give a good idea of the material resistance to stress corrosion cracking (SCC). The absorption tower is welded together, which can create stressed areas. austenitic stainless steel 304L was compared to 316L.

- The result from the analysis of the corrosion behaviour of the 316L stainless steel and the materials tested for comparison will aid in material selection for future H_2S cleaning stations and maintenance planning.

In chapter 2 several types of H_2S abatement systems, the sulfix project and corrosion in H_2S environments are introduced. Chapter 3 introduces the theory behind the results derived from this experiment. Several types of different corrosions that might be expected and introduces the equipment necessary to get the results. Chapter 4 is an introduction on the materials chosen to be tested in this experiment. Experimental setup, design of the specimens and handling is detailed in Chapter 5. Chapter 6 details the results from different time periods used in this experiment, both for coupon and U-bend samples. In Chapter 7 the results are discussed and the thesis is concluded in Chapter 8 where the main contributions from this experiment are highlighted.

2. Background

2.1. H$_2$S cleaning from geothermal steam

Stephens et al. (1980) describe two stages where the removal of H$_2$S in a geothermal system can take place, before the steam flow enters the turbine (upstream) and after the turbine (downstream). Sanopoulos & Karabelas (1997) classify the abatement systems into four methods, based on Stephens et al. (1980) description and the type of flow. Table 2.1 describes the four methods used and Figure 2.1 shows location for each process in a power plant.

Table 2.1: Description of methods for H$_2$S abatement processes.

Method	Location	Type of flow
Method A	Upstream	Geothermal steam
Method B	Downstream	Off-gas ejector
Method C	Downstream	Condensate water
Method D	Downstream	Combinations of flows

Source: (Chaves, 1996)
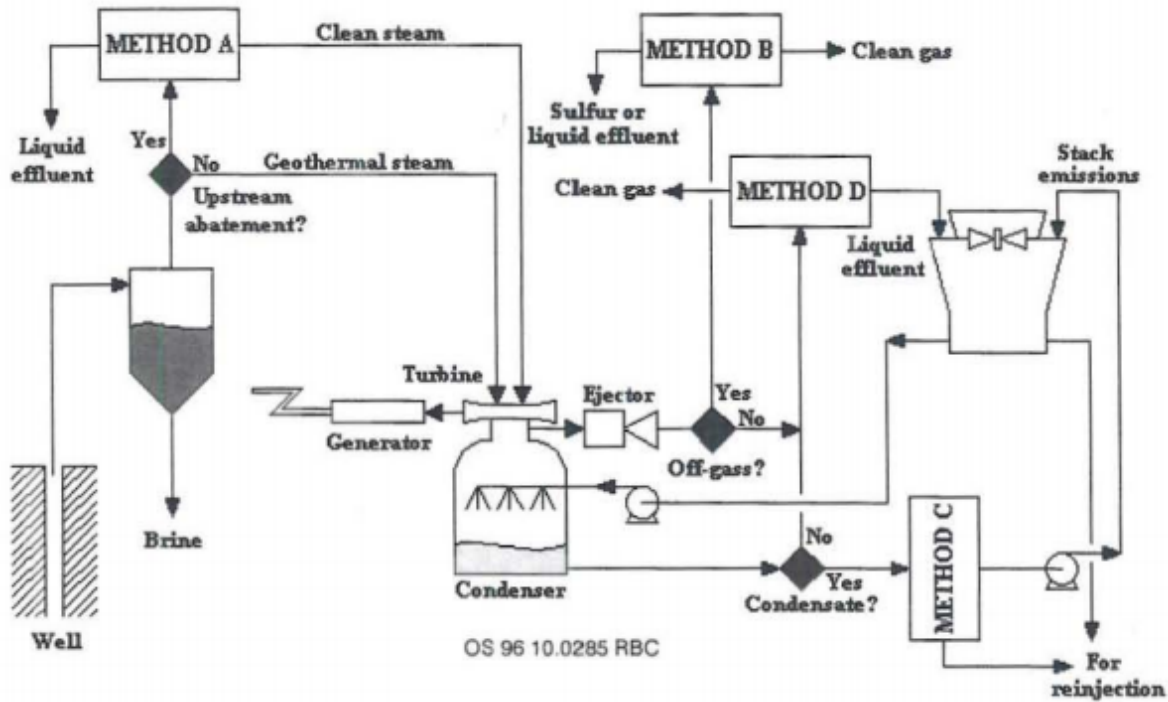
Figure 2.1: General classification of the H_2S abatement processes.

Source: (Chaves, 1996; Sanopoulos & Karabelas, 1997)

The upstream method A is a processes that has never been tested and verified on geothermal power plants, this method has the theoretical potential of increased power generation due to non-condensable gases elimination and protection to the turbine components from corrosion, scaling and erosion. The main set-back from this method is the thermal energy loss in the elimination process. There are two H_2S abatement alternatives listed for Method A. Direct treatment to the total amount of geothermal steam to remove H_2S and separation of the non-condensable compounds from the geothermal steam and further treatment of these compounds with appropriate processes (Sanopoulos & Karabelas, 1997). Method B ejects the non-condensable gases in the condenser and extracts H_2S from the mixture, normally with chemical methods. Method C is a so-called "secondary abatement", where dissolved or partitioned H_2S in the condensate is removed before entering the cooling tower. This method is normally used in combination with other methods. Method D is a hybrid system capable of treating both the condensate stream and the downstream gas to eliminate H_2S emissions (Chaves, 1996). Many H_2S abatement processes have been developed during the last four decades, all of them can be classified into Methods from A-D. There is a complicated process of selecting the right abatement system to a power plant due to variations of geothermal fields and geothermal fluids on different geothermal locations. Each process has its unique feature and different advantages and disadvantages are linked to each method (Sanopoulos & Karabelas, 1997). Three power plants operating H_2S abatement systems are introduced in this section.

H_2S abatement systems have been successfully operated at the Geyser geothermal field in California. Over the past 50 years they have played an important role in the growth and development of geothermal utilization in the area. In the 1970's H_2S emission rules were applied in the United States, as an example, 396 MW produced in 1974 emitted about 700 Kg/hr of H_2S into the atmosphere while the annual average emission for 2007-2010 of total 750 MW was about 57 Kg/hr. Technique used at Geyser geothermal field are of two types, Dow-Spec RT-2 (Method D), an hybrid abatement system forming the soluble thiosulfate by-product and the Stretford process (Method B), proven to be successful for over 30 years, which converts H_2S to sulfur with air oxidation (Farison et al., 2010).

Yanaizu-Nishiyama Geothermal power plant, a 65 MW station located in Japan installed an H_2S abatement system that started operating in 1998. Complaints of odor in the air was the driving force of installing such a system and an environmental friendly process was the primary goal. Amount of non-condensable gases in the steam were about 6 wt%, which is considered to be high, emitting total of 500 m^3/h of H_2S. In 1996 the power output of the plant was reduced to 34 MW during a investigation to identify the location of the source, during that time the H_2S emission reduced to 340 m^3/h. The power plant was the first geothermal power plant in the world to use a combination of Selectox and Claus processes (Method B) for H_2S elimination, where the by-product molten sulfur is generated with the help of two Selectox reactors, one Claus reactor and catalysts (Takahashi & Kuragaki, 2000).

Coso geothermal field in California operated a unsuccessful non-condensable gas injection system for nearly 7 years, where non-condensable gases were mixed with the brine and re-injected underground, similar to the technique used at Hellisheiði geothermal power plant. However, this system slowly faded out due to several problems, such as, corrosion in gas lines and well casings, vapor lock at the re-injection wells and gas breakthrough in the field. It is also reported that the re-injection started to affect the performance of the reservoir (Nagl, 2009). It is believed that this method could be successful for small facilities with low non-condensable gases concentration. Coso geothermal field has two power plants sites and it was decided to eliminate H_2S with liquid redox processes (Method B) converting it to the elemental sulfur. Using Lo-Cat and SulFerox units. The two SulFerox units produced 17.8 tons per day at the so-called BLM-site of the geothermal field. After three months of operation problems were encountered, such as, line fouling and plugging as well as seal failures on the pump for both SulFerox and Lo-CAT systems due to the solid sulfur contained in the liquid. It is reported that operators were not comfortable with the performance of SulFerox units (World Environment Center, 1994). Nagl (2009) reports a 15 year success of the three Lo-Cat units used at the Navy-site of the Coso geothermal field, consistently showing efficiencies above 99.99% of H_2S removal by oxidizing H_2S to the elemental sulfur.

2.2. The SulFix project

The aim of the SulFix project is to dispose H_2S gases with economic, efficient and environmental ways. Due to new legislation in Iceland, nr. 514/2010, about H_2S emissions into the atmosphere. Three power companies in Iceland, utilizing geothermal power made an mutual agreement in 2012 on finding ways of fulfilling this new legislation. These companies are Orka Náttúrunar (subsidiary of Orkuveita Reykjavíkur), Landsvirkjun and HS Orka. Orkuveita Reykjavíkur had previously been working on another project, CarbFix which started in 2007 where the goal was to dispose CO_2. Through the experience of the CarbFix project, valuable information was contributed to this project. The SulFix project is split into five main phases, 0-4, and according to plan, Hellisheiðarvirkjun should be able to run a fully developed H_2S abatement system in 2020 capable of disposing 50% of all H_2S from the plant.

This experiment was performed when the SulFix project was in phase two. It is estimated that the system dissolves 98% of the H_2S gases along with 57% of the CO_2 gases in condensed water (Gunnarsson et al., 2015). "Verkefnisáætlun SulFix: Um förgun brennisteinsvetnis frá jarðgufuvirkjunum" (2013), a report from the power companies about the SulFix project estimated that 15-30% of all the gases from Hellisheiði Power Plant goes through the air cleaning system in phase two. The condensed water with dissolved gases is re-injected into the ground at approximately 700m below the wellhead where the reservoir temperature is around 200-270°C (Gunnarsson et al., 2015). Simulations show that injected H_2S is sequestered into pyrrhotite, one of mineral buffers in the aquifer controlling H_2S concentration in geothermal systems. The simulations also show that the re-injection of H_2S under Icelandic geological and thermal conditions are a viable option (E. S. Aradóttir et al., 2012). Thus, it can be expected that the re-injection at Hellisheiði power plant should not encounter problems such as reported at the Coso geothermal field (World Environment Center, 1994). Furthermore, it is predicted that in 1-5 years after the re-injection both the CO_2 and H_2S gases have mineralized for long term storage in the subsurface (E. S. P. Aradóttir et al., 2015).

2.3. Corrosion in H_2S environments

Corrosion is well known in the oil and gas industry and similar to geothermal environments they can contain hydrogen sulfide (H_2S), carbon dioxide (CO_2) and chloride (Cl^-). Therefore many corrosion researches made for the oil and gas industry are relevant to corrosion in geothermal industry. Moreover, austenitic stainless steels are commonly used materials in the oil and gas industry in the presence of H_2S. This section introduces some researches focusing on austenitic stainless steel 316L in an environment exposed to H_2S.

Ding et al. (2013) studied the corrosion behaviour of austenitic stainless steel 316L. Particularly SCC, in high H_2S-CO_2-Cl^- environment. The alloy was tested with the four-point

bending test method at 60°C under high pressure of H$_2$S-CO$_2$ with 150,000 ppm Cl$^-$. The effects of high H$_2$S-CO$_2$ pressure was discussed and the test shows that higher H$_2$S-CO$_2$ pressure increases the corrosion rate, more corrosion products precipitate, deterioration of passive film occurs and the corrosion process accelerates. Also, large localized corrosion areas can be found on the edges of the specimens, initiating SCC with deep and thick cracks. The corrosion behaviour of the alloy was tested using cyclic potentiodynamic polarization measurements where the effect of pH on pitting corrosion was discussed, the test shows that lower pH leads to higher corrosion rate due to the acceleration of both cathodic and anodic reactions, furthermore it shows changes on the the passive film layer from passive state to active where the passive films break downs and pitting corrosion initiates.

He et al. (2009) studied the synergistic effects of high concentration of chloride and H$_2$S on the oxide formation and metal dissolution on austenitic stainless steel 316L. Experiments were carried out at room temperature 20-23°C in an simulated environment where NaCl solution with combined H$_2$S and CO$_2$ gases were used to simulate conditions found in gas and oil pipelines. Results from this experiment suggested that the combination of H$_2$S and NaCl have synergistic effects on the oxide layer formation. However H$_2$S is not believed to interact directly with the oxide layer and tear it down as strongly as Cl$^-$ but from H$_2$S the sulfur element probably enters the metal surface through oxide layers weakening and forms metal sulfides, thus the oxide layer becomes more defective.

Lu et al. (2005) show with slow strain rate tests on 316L stainless steels in H$_2$S and Cl$^-$ aqueous solutions that chloride ions are more effective to SCC than H$_2$S. This is shown by testing the alloy under different concentrations of H$_2$S and Cl$^-$.

Prakash et al. (1999)performed a laboratory experiment studying SCC of alloys exposed to corrodents such as chloride, oxidants and H$_2$S. Prakash et al. (1999) determined the threshold for SCC on several alloys used in desalination plants, including 316L. The experiment was made at ambient temperature and included investigations on round and flat samples under tensile condition. Two different solutions were used, bubbling with H$_2$S to maintain H$_2$S saturation, one of the solutions contained 5% of NaCl. The effects of electrochemical potential on intergranular SCC was tested in five different solutions, containing either H$_2$S or Cl$^-$ or both. Prakash et al. (1999) experiments found 316L to be immune under all test conditions, showing that 316L could be an ideal material selection in desalination plants at ambient temperature.

Davoodi et al. (2011) compared austenitic stainless steels 304L and 316L in acidic H$_2$S concentrated media, with pH = 3 and the temperature at 60°C. Different concentration were tested, respectively 0, 5 and 15 ppm. The study shows that for increased H$_2$S concentration the corrosion resistance diminishes for both alloys as well as the current density for both alloys increases. Interesting discovery was made where for high concentration of H$_2$S, 15 ppm. The study shows that 304L has better corrosion resistance than 316L. 304L produced FeS$_2$ at the surface while 316L produced a combination of FeS$_2$ and MoS$_2$ where the molybdenum in 316L could cause sulfur species detachment at the surface leading to a thinner surface layer.

3. Theory and methods

In this chapter methods and theories relevant to this research are discussed. This chapter is divided into two categories. Corrosion theory and methods used to determine and estimate the corrosion.

3.1. Corrosion theory

Most metals are unstable in the atmosphere and when exposed to it they tend to return to their original state or similar metallic compounds. The simplest definition on corrosion is the process of a metals returning to their thermodynamic state (Schweitzer, 2010). Metallic corrosion is almost always an electrochemical process which involves two half cell reactions. Oxidation reaction at the anode and an reduction reaction at the cathode. Electrical connection is essential, allowing electrons to flow from the anode to the cathode. Also a conducting environment for the flow of ions is needed. All corrosion reactions include an anodic reaction and one or more cathodic reactions (Roberge, 2008). Thus, when a metal is exposed to a corrosive media, the media connects the anode to the cathode and the anode loses electrons that are absorbed by the cathode. The cathode is constantly attempting to balance its positive or negative charges (Popoola et al., 2013) and therefore absorbing electrons from the anode.

Typical anodic reaction is an oxidation process where electrons get liberated and these reactions can be written in the general form which applies to all corrosion reactions:

$$\mathbf{M} \rightarrow \mathbf{M^{n+}} + \mathbf{ne^{-}} \tag{3.1}$$

where the corrosion of metal M is an oxidation process from metal to an ion with a charge of $n+$ and n is the number of electrons released (Jones, 1996; Roberge, 2008).

Cathodic reaction depends on the environment the metal gets exposed to. Roberge (2008) lists up several cathodic reactions that can be encountered during corrosion of a metal (equations 3.2 - 3.4) combined with the cathodic reaction that could be expected in an hydrogen sulfide solution (equation 3.5).

$$(\text{acid solutions}) \quad O_2 + 4H^+ + 4e^- \rightarrow 2H_2O \tag{3.2}$$

$$(\text{neutral or basic solutions}) \quad O_2 + 2H_2O + 4e^- \rightarrow 4OH^- \tag{3.3}$$

$$\text{(Hydrogen ion reduction)} \quad 2H^+ + 2e^- \rightarrow H_2(g) \tag{3.4}$$

$$\text{(Hydrogen sulphide ion reduction)} \quad 2H_2S + 2e^- \rightarrow 2HS^- + H_2(g) \tag{3.5}$$
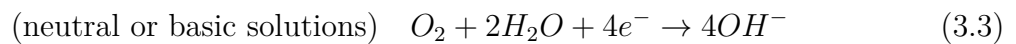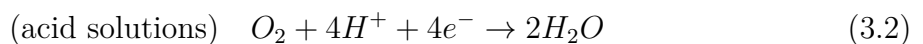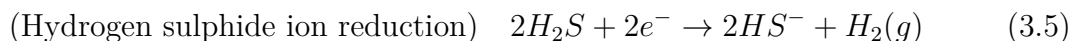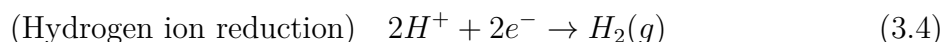
Oxygen reduction is a common cathodic reaction since a metal can be in an atmospheric environment or a solution exposed to the atmosphere (equations 3.2 and 3.3). Another common cathodic reaction takes place in acidic environments. That is when hydrogen ions combine as their ions reduce and form a balance disturbance of ions between acidic hydrogen (H^+) and alkaline hydroxyl (OH^-), making the solution less acidic (equation 3.4). This applies for several types of metal ions including the reduction of hydrogen sulfide ions which is relevant to this experiment.

Corrosion occurs in several forms. In this chapter the basics behind the film on the surface of metals are discussed before corrosion forms that might be expected in this experiment are introduced.

3.1.1. Corrosion film

Metals that lose one or more of their electrons from the metallic bond transforming a metal to a metal ion are experiencing corrosion. These reactions produce a by-product called corrosion product, a film on the surface of the corroded metal. These films are, for example, insoluble hydroxides, oxides, carbonates, sulfides, silicates and borates. They can be porous and loose, allowing diffusion to and from the metals surface resulting in further corrosion. Also, they can be non-porous, tight and adherent, limiting access of corrosives to the metals surface and protecting the metal from corrosion.

Corrosion can be active or passive. Active corrosion can occur in some environments where corrosion products are very soluble and form no corrosion film on the surface of the corroding metal (Karlsdóttir, 2012). Many metals, however, under specific humid or liquid oxidizing conditions with high anodic polarization undergo a procedure called passivity. A passive corrosion, where they form a thin compact oxide film on the surface, creating a barrier between the metal and its environment. Thus, protecting the metals from corrosion. Most of the commercial corrosion resistant alloys depend on the passive film due to their corrosion resistant (Landolt, 2007).

In order to understand this the process it is necessary to understand the term anodic polarization in general. Anodic polarization is the process of corrosion and oxidation, that is, a corroding or oxidizing metal. Electrons from the metal are liberated creating a positive surface potential change which is the driving force for corrosion and oxidation. The power of corrosion and oxidation increases when the positive surface potential change increases due to higher anodic polarization. Metals with added iron, nickel, chromium, titanium and cobalt have a critical point E_p, where under the right conditions e.g. 316L

stainless steel in aerated environment the positive surface potential changes the metal to an passive state as can be seen in Figure 3.1. The Figure shows an gradual increase in corrosion rate due to increased current flow of electrons. At point E_p the current drops dramatically and slows down the corrosion rate significantly. For 316L stainless steel in aerated environment there would be an oxidation process, creating a passive Cr_2O_3 film on the surface (Jones, 1996).
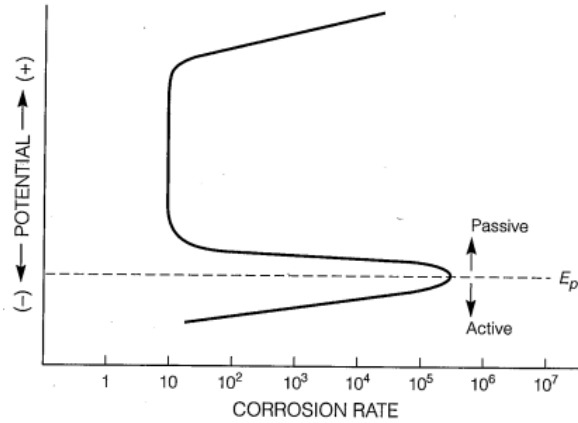
Figure 3.1: Anodic polarization curve for metals with active-passive behaviour.

Source: (Jones, 1996)

3.1.2. Uniform corrosion

The most common form of corrosion is uniform corrosion, where the metal dissolves uniformly over the exposed surface (Jones, 1996; Schweitzer, 2010). The corrosion attack occurs in a situation where anodic and cathodic areas on the surface of the metal keep shifting, making the corrosion uniformly distributed over the surface. With time the metal becomes to thin to be operable and fails, thus, precautionary maintenance is needed to replace the corroded component (Javaherdashti et al., 2013). Uniform corrosion is a predictable form of corrosion and can be easily measured with weight loss methods (Karlsdóttir, 2012). In geothermal systems uniform corrosion often occurs in the presence of chloride (Cl), carbon dioxide (CO_2), oxygen (O), hydrogen sulfide (H_2S), ammonia (NH_3) or when acidity increases (pH decreases) (Conover et al., 1980; Kaya & HoShan, 2005).

3.1.3. Pitting corrosion

Pitting corrosion is a localized loss of metal on the surface. It is a unpredictable form of corrosion which leads to sudden failure of passive metals and alloys. This often rapid

loss of metal in a small area results from localized breakdown of its passive layer oxide film, creating pits or holes on the surface. The pits can be seen in different shapes and sizes, such as, narrow, elliptical, deep, wide, shallow, undercut or subsurface (Jones, 1996). Non-passive alloys with protective coating in a certain environment can take up this form of corrosion (Sprowls, 1987). Stainless steels, aluminium and their alloys are very susceptible to pitting in neutral- to acid chloride solutions due to local breakdown of the passive film. In these chloride environments, increased temperature and dissolved oxygen increases the susceptibility for pitting. However, high temperature can also reduce the risk of pitting due to decreased solubility of dissolved oxygen as well as high velocity flow (Jones, 1996; Schweitzer, 2010). It has been shown that stagnant conditions have significantly more impact on the formation of pits than high velocity flow (Karlsdóttir, 2012; Schweitzer, 2010). The addition of chromium (Cr), molybdenum (Mo) and nitrogen (N) to an alloy can decrease the alloys susceptibility to pitting. As a result, the measure for pitting corrosion resistance of an alloy can be described with equation 3.6 which quantifies their respective contribution to the pitting resistance. The result is the pitting resistance equivalent number (PREN), where higher PREN values indicate a greater pitting resistance (Schweitzer, 2010).

$$PREN = \%Cr + 3.3(\%Mo) + 30(\%N) \tag{3.6}$$

It can be difficult to detect pitting corrosion during inspection due to their small size and that fact that corrosion products on the surface can cover the pits opening (Schweitzer, 2010). also, different shapes and sizes of the pits make it difficult to evaluate the extent of pitting (Jones, 1996). Weight loss measurement is not considered to be a good indication on the extent of pitting unless the pitting is severe and uniform corrosion is in considerably small amount (Sprowls, 1987).

3.1.4. Stress corrosion cracking

Stress corrosion cracking (SCC) is an unpredictable and severe failure occurring under static tensile stress often with the presence of specific chemical, such as chloride ions in the environment. The most common compounds promoting SCC are chloride and hydrogen sulfide (Papic, 1991). SCC susceptibility to metals is controlled by the metals structure and composition, stress, and temperature. If the metal is exposed to a fluid the composition of the fluid and pH value are very important. For austenitic stainless steels, increased oxygen and chloride concentration in the solution increases the metals susceptibility to SCC and increased temperature increases the acceleration of the corrosion (Conover et al., 1980; Karlsdóttir, 2012). In the presence of corrosion, the threshold stress for SCC can be as low as 10% of the metals yield stress. Usually the metal or alloy is free of corrosion on the surface except for the point of stress, fine cracks penetrate through the surface either intergranular or transgranular. However, intergranular cracks are more common, perpendicular to the applied stress. For most industrial applications,

the progress of SCC is slow and difficult to detect, leading to an unexpected failure. It is important that all stresses induced by fabrication is removed. Stresses can be either residual or applied, such as welding, bending or faulty installation (Jones, 1996; Schweitzer, 2010). In geothermal applications, SCC is the most dangerous form of corrosion (Corsi, 1986).

3.1.5. Sulfide stress corrosion cracking

Sulfide stress cracking (SSC) in metals occurs under stressed conditions in an environment exposed to H_2S in aqueous phase. High strengthen steels are more susceptible to SSC and the rule of thumb is to limit the use of steels with hardness 250 HV (Vickers hardness) or more. In geothermal systems with low pH value the SSC mechanism accelerates the failure of components. SSC is an unpredictable form of corrosion with sudden and severe failure to the component. Increased temperature and pH level decrease the effects of SSC and oxygen seems to have little or no effects on this corrosion mechanism (Conover et al., 1980). SSC is less common in geothermal industry compared to oil and gas due to the high temperature of geothermal fluids (Corsi, 1986).

3.1.6. Hydrogen induced cracking

Hydrogen atoms (H) are the smallest atoms found in the periodic table and because of that they can diffuse into the metallic structure of metals and alloys and recombine to form a molecule as seen in eqation 3.7 (Roberge, 2008).

$$2H^0 \rightarrow H_2(g) \tag{3.7}$$

For low-strength steels the combination of two hydrogen atoms into an molecule can cause high internal pressure which causes blisters and fissures on the metal surface. This is often referred to as hydrogen blistering (HB). In high-strength steels this corrosion mechanism causes cracks as the hydrogen content and pressure increases inside the high-strength alloy the ductility decreases. This is often referred to as hydrogen induced cracking (HIC) (Roberge, 2012). H_2S is a common hydrogen source in geothermal applications and in contact with iron the release of hydrogen can be expressed with equation 3.8 (Schweitzer, 2010).

$$Fe + H_2S \rightarrow FeS + 2H \tag{3.8}$$

3.2. Methods and equipments

In order to analyze the corrosion products on the tested samples and evaluate their corrosion rate it is necessary to use standard corrosion measuring techniques and use microscopic analysis as described in this chapter.

3.2.1. Corrosion rate and pitting

To estimate the corrosion rate specimens are weighed before installation and exposure to the corrosive environment for a period of time. After exposure specimens are weighed and cleaned following standard ASTM G1-90 (1999). Final weighing of the specimens is when the specimen is free of corrosion products. From the initial and final weight of the specimen the corrosion rate, CR [mm/yr] can be calculated with equation 3.9

$$\frac{8.76 \times 10^4 \cdot \text{W}}{\text{A} \cdot \text{T} \cdot \rho} \tag{3.9}$$

where the constant 8.76×10^4 is a specific unit described in standard ASTM G1-90 (1999) for the formula to give the result in mm/yr. W [g] is the weight loss of the specimen, A [cm^2] is the surface area of the specimen exposed to the environment, ρ [g/cm^3] is the density of the material tested and T [hours] is the time the specimen was exposed (time of the test) (Jones, 1996).

For this specific case coupons were used as described later in this thesis. The surface area of the coupons in contact with its environment is calculated with equation 3.10

$$A\,(\text{cm}^2) = \frac{\pi(D_{\text{mm}} \cdot h_{\text{mm}} + (\frac{D_{\text{mm}}^2 - d_{\text{mm}}^2}{2}))}{100} \tag{3.10}$$

Where D is the diameter of the coupon ($\approx$ 45 mm), d is the diameter of the insulator ($\approx$ 15 mm) blocking part of the surface from the environment and h is the thickness of the coupon ($\approx$ 3 mm). For accurate results, specimens should be in similar shapes and sizes, kept as thin as possible with a large surface area (Ragnarsdóttir, 2013). The acceptable corrosion rate limit is generally considered to be 0.1 mm/yr (Lichti et al., 2010).

Localized corrosion can not be measured with the corrosion rate method described above, there for, specimens are examined under instructions from standard ASTM G46-94 (2013) where in case of pitting, the density, shape, depth and size of the pits will be reported.

3.2.2. Constant deformation test (U-bend)

U-bend method is a simple and effective way to determine the SCC resistance of alloys under different scenarios, such as, different types of alloys in the same environment, different metallurgical conditions of an alloy in the same environment or an alloy under constant conditions in different types of environments (Prakash et al., 1999). U-bend specimens are made by plastically deforming a sheet or a bar over a mandrel (usually 180°) and the ends are bolted together to sustain the strain. With this method stress distribution within the specimen is not well known and it is difficult to duplicate the conditions from specimen to specimen. However, this method is quite convenient experimentally and forms one of the most severe smooth specimen tests for SCC (Jones, 1996).

When a sheet or a bar is deformed into U-bent specimen the outer surface of the samples are stressed into plastic region where the total strain ε is given with equation 3.11

$$\varepsilon = \frac{T}{2R} \quad \text{When} \, T << R \tag{3.11}$$

where T = specimen thickness and R the radius of the bend. Section 5.4 describes the forming of U-bent specimens used in this experiments according to standard ASTM G30-97 (2009).

3.2.3. SEM and XEDS

The scanning electron microscope (SEM) is a popular tool capable of providing high depth three-dimensional-like images of the surface of various types of materials under high magnification, for example enabling the evaluation of its microstructure. The SEM is a complex tool, firing electrons on the specimens surface that interacts with the specimen and creates signals which are detected by detectors, these signals are used for image scanning and can carry the information of the materials composition, shape, surface texture amongst other things. It is necessary that the electrons get a free flow, therefore the specimens are put into a vacuum chamber where the pressure is reduced to about 10^{-5} Pa. At that pressure only 1 electron out of 10,000 collides with the few gas molecules in the chamber and are deflected out of the beam. With an equipment addition the SEM can also be used to obtain the localized chemical composition of the material using x-ray photons generated by the electron beam. These x-ray photons emerging from the surface of the specimen contain energies specific to the elements in the specimen and can thus give information on the composition. The x-ray energy dispersive spectroscope (XEDS) is an analytic technique which detects and measures the x-rays and combined with SEM it can give chemical analysis for multiple areas with different sizes on the same image on the surface of the sample (Goldstein et al., 2003).

4. Material selection

Material selection is a crucial part of the design. Geothermal fluids can contain dissolved CO_2, H_2S, NH_3 and chloride ions which can be a very aggressive environment causing corrosion of metallic materials (Kaya & HoShan, 2005). Correct material selection involves the cost aspects as well as lifetime and safety aspects of the product. In this chapter materials used in this experiment are introduced.

The metals chosen were carbon steel S235, a popular metal with low corrosion resistance but is easy to fabricate and not expensive, it was chosen for comparison to 316L because it is a lower grade metal and was expected to corrode. Stainless steel 316L was chosen becuase it is currently used in the H_2S abatement systems absorption tower at Hellisheiði geothermal power plant. Stainless steel 304L was chosen because it is a lower grade metal to 316L and is not considered an material option in design at Hellisheiði according to the lead designer of the H_2S abatement system. Duplex stainless steel 2205 is also used in this experiment, an alloy that can be considered to be the next material choice after 316L. For example, Duplex 2205 was successfully used at Svartsengi power plant in Iceland after severe pitting corrosion of valve stems made of both 13% Cr steel and hard chromed steel(Thorolfsson, 2005).

Chemical composition of the chosen materials are summarized in Table 4.1.

Table 4.1: Chemical composition of the materials used in this experiment.

Material	C (max)	Si(max)	Mn (max)	P (max)	S (max)	Cr	Ni	Mo	Other	Fe
					Chemical composition [%]					
S235	0.22	0.05	1.6	0.05	0.05	-	-	-	-	Bal.
304L	0.03	0-1	0-2	0-0.05	00-0.02	17.5-19.5	8-10.5	-	-	Bal.
316L	0.03	0-1	0-2	0-0.05	0-0.01	16.5-18.5	10-13	2-2.5	-	Bal.
2205	0.03	0-1	0-2	0-0.03	0-0.02	22-23	4.5-6.5	3-3.5	N=0.14-0.2	Bal.

Source: (Aalco, 2015a,b; Gilbert, 2014; Materials, 2014)

4.1. Carbon steel

Carbon steels are commonly used in the geothermal power plants, their reliability varies depending on their application in the power plants. Due to their availability, low cost and fabrication availability carbon steels are an attractive material and most geothermal systems use them in a large scale in various applications. Their applications in geothermal power plants can be wellheads, pipelines, separators, flash units and turbine rotors. In geothermal power plants carbon steels usually undergo localized and uniform corrosion, thus the metal is mainly used in thick walled applications where thinning by uniform corrosion is accounted resulting in a longer lifetime of the part. The resistance for corrosion is though limited to low pH, high chloride concentration and high flow rates. One of the main reasons carbon steel was selected in this experiment was because that geothermal systems are composed and manufactured largely of carbon steels and in many of these applications they server well (Karlsdóttir, 2012).

4.2. Stainless steel

Stainless steels can be divided into 6 groups (Roberge, 2012). In the following subsections two of those groups that were used in this experiment are introduced, austenitic stainless steels such as 304L and 316L as well as the duplex stainless steel 2205. Steels with 10.5% Cr are categorized as stainless steels, the chromium content forms a passive chromium oxide layer on the surface resulting in increased corrosion resistance. However, localized corrosion can occur if the passive film breaks, e.g. pitting corrosion, crevice corrosion and cracking causing damages.

4.2.1. Austenitic stainless steel

Austenitic stainless steels are the most common type of stainless steels used and usually contain 18% Cr and 8% Ni. Corrosion resistance can be enhanced with the addition of chromium, molybdenum and nitrogen.

This non magnetic alloy can be graded with the letter L, which indicates that the alloy is low in carbon. The carbon content of the alloy is kept at 0.03% or less to avoid chromium carbide (Cr_3C_2) precipitation at the grain boundaries (Roberge, 2012). According to Conover et al. (1980) austenitic steels tend to be immune to SSC but at temperatures higher than 60°C in an chloride solution stress corrosion cracking might occur.

The manufacturer (Sandvik) reports that 304L and 316L are susceptible to SCC at temperatures over 60°C if the steel is subjected to tensile stress in contact with chloride solutions. 316L has higher pitting resistance than 304L due to the molybdenum content

in the alloy. In flue gases containing sulfur, corrosion resistance is reduced for both metals (Sandvik, 2015b,c).

4.2.2. Duplex stainless steel

The newest group member of the stainless steel family, duplex stainless steel, with two major microstructures phases, ferrite and austenite giving them high resistance to SCC in chloride solutions (Roberge, 2012).

Duplex stainless steel 2205 is an overall better corrosion resistant alloy compared to the austenitic stainless steels used in this experiment. The manufacturer (Sandvik) reports that 2205 is high corrosion resistant in chloride and hydrogen sulfide containing environments and that the alloy can be used at higher temperature and with higher chloride content than standard austenitic steels without pitting. It is also stated that they are less prone to be susceptible to SCC (Sandvik, 2015a).

5. Corrosion experiment

This experiment was made to evaluate the corrosion resistance of the absorption tower which is in contact with high concentrations of H_2S, the tower is made out of 316L stainless steel and is operating at Hellisheiði, Iceland.

5.1. Experimental design and setup

The specimen holder used for this experiment was capable of carrying both the coupon and U-bent specimens. Mannvit engineering designed the specimen holder used, see Figure 5.2a, schematic design can be viewed in Appendix C in Figure C.1. The Specimen Holder was put into H_2S rich area located at 2nd floor in the air cleaning stations absorption tower, see Figure 5.1.
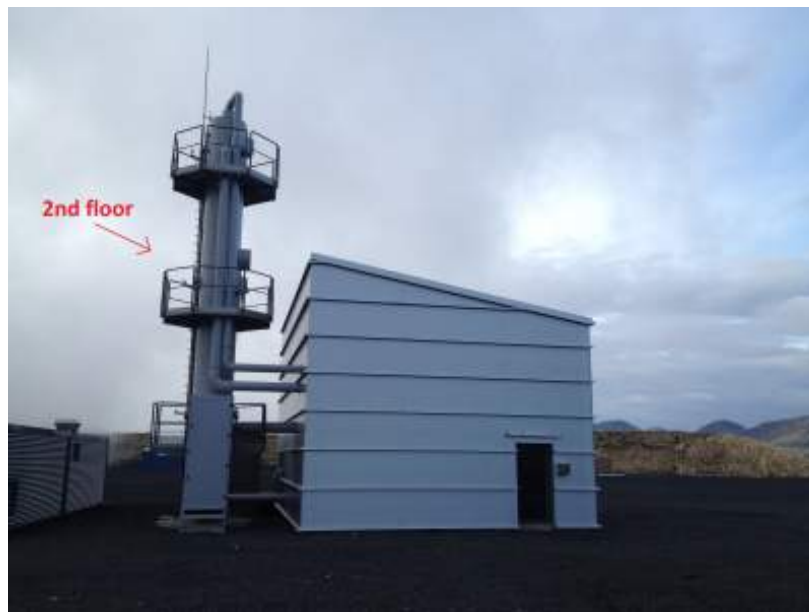
Figure 5.1: Air cleaning station with the absorption tower to the left of the building.

The specimen holder was designed to be able to put the specimens into the tower while it was operating in the safest way possible. A valve on the tower with threaded pipe

matching the thread on the specimen holder is the key for this to be possible, the valve and threaded pipe can be seen on Figure 5.2b. The specimen holder was screwed onto the pipe, then the valve on the tower was opened with high safety, the pressure in the tower is 5 bars and the specimen holder reduces the risk of releasing H_2S into the air near the operator. When the valve was opened the 20 mm axle that goes through the specimen holder was pushed so that the specimens got into desired position in the tower, see Figure 5.2c, at the end of the specimen holder there is an airtight seal, to prevent H_2S leakage through the 20 mm axle. On the specimen holder there is a valve, for safety, it needs to be closed when the specimen holder is inserted and in the tower. After the testing period had expired and specimens were being collected from the tower the valve on the specimen holder was opened after the specimens had been pulled back and the main valve on the tower had been closed. After the main valve on the tower had been closed the specimen holder was isolated from the tower, however, the specimen holder still had 5 bars of H_2S contaminated pressure inside. The valve on the specimen holder was opened carefully and the pressure got released for safe specimen holder withdraw.

(a) Specimen Holder with test samples, see valve on the bottom left.
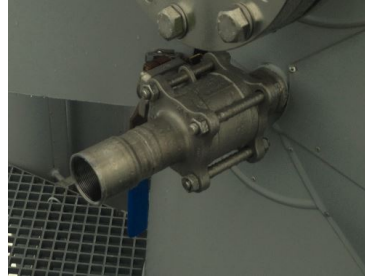
(b) Valve before mounting the Specimen Holder in closed position.

(c) Specimen Holder screwed onto the main valve and inserted.

The absorption tower operates at 5 bar as mentioned earlier and has a temperature around 20-25°C. Condensed geothermal water is pumped into the tower near the top at 34-36 l/s and non-condensable gases are compressed in near the bottom, approximately at the rate of $0.4 - 0.5$ kg/s. See Figure 5.3. The absorption towers purpose is to get rid of the less soluble gases such as H_2, N_2, CH_4 and Ar prior to the re-injection. These gases can built up pressure in the injected aquifer, leading to an expensive disposal method due to extensive amount of water needed to complete the dissolution of all the gases or inhibit the dissolution of H_2S and CO_2 (Gunnarsson et al., 2015). Prior to the absorption tower the condensate is cooled from 45°C to 20°C to increase the solubility of the gases in the water

The specimen holder was inserted in a valve located near the middle of the station. At that specific point the concentration of H_2S in gas phase has lowered because of the mechanism of the absorption tower. Some of the H_2S has dissolved on the way up the tower because it has gone through the first stage of the dissolution process. Below and above the specimen holder is a grid mechanism that forces the gas to get into contact with the condensed water so that the H_2S and CO_2 gases dissolve into the liquid. Higher

pH value and lower H_2S concentration can thus be expected, but is not measured at that specific location.
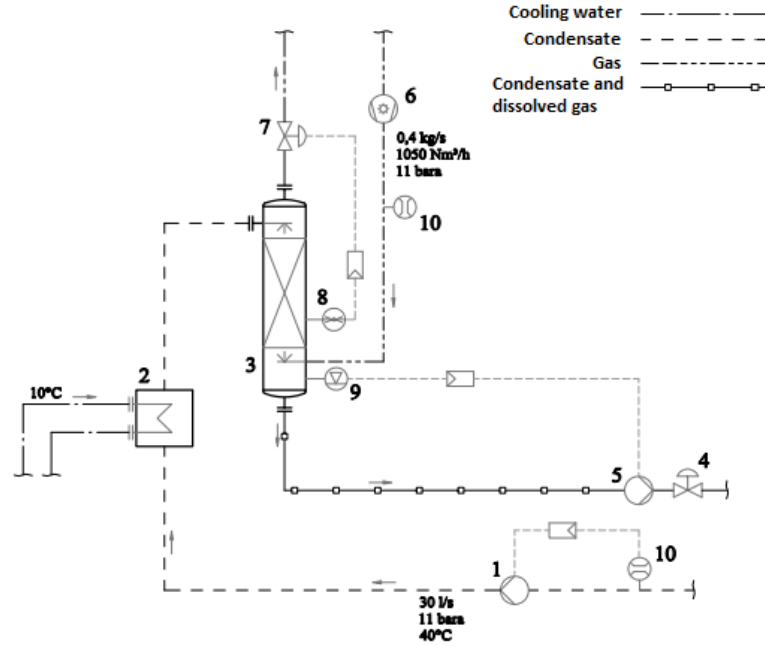
Figure 5.3: Description of the air cleaning system.

Samples are taken near the injection well, before the gas reaches the air cleaning station and on the top of the absorption tower where the gas goes out to the atmosphere at an estimated pH value of 5.5. These samples are taken on a regular basis and were provided by Orkuveita Reykjavíkur (OR). Average chemical compositions of the gases before entering the absorption tower and of the gases going from the tower can be seen in Tables 5.1 and 5.2. The composition in the condensed water after absorption and before re-injection can be seen in Table 5.3. The condensate with the dissolved gases is considered to have a pH $\approx$ 3 (Gunnarsson, 2015). Tables for all available chemical composition can be found in Appendix A, Tables A.1 to A.3. The Tables 5.1 to 5.3 show the conditions before and after the absorption tower and show what environments could be expected for the materials tested.

Table 5.1: Average chemical analysis of gases before the absorption tower [% of volume].

H_2	O_2	N_2	CH_4	CO_2	H_2S
16.6	1.3	6.2	0.4	56.4	24.0

Table 5.2: Average chemical analysis of gases going from the air cleaning station [% of volume].

H_2	O_2	N_2	CH_4	CO_2	H_2S
34.6	1.5	8.1	0.9	52.5	2.7

Table 5.3: Condensed water after the absorption tower [ppm].

CO_2	H_2S
4298.8	2387.5

The Tables show that some oxygen is present for the gas going into the absorption tower which should be taken into concerns, specially since the weight percentage of the oxygen level and the other non-condensible gases are expected to increases with a gradient the further it goes up the tower as H_2S and CO_2 dissolves in the condensate. No chemical analysis exists for the condensate but it is expected to be like distilled water with about 1 ppm dissolved CO_2 and H_2S before it reaches the absorption tower (Gunnarsson, 2015). Table 5.3 shows that the condensed water is rich with H_2S and CO_2 after the dissolution process.

The experiment was divided into three periods. First two experiments were 4 weeks tests and the third was an 12 week experiment. Time plan can be seen in Table 5.4. Because of the variance in performance of the system for the first 4 week test it was decided to repeat the test again if the performance variance would have any impact on the results.

Table 5.4: Time schedule for the corrosion experiments [weeks].

Week	1 2 3 4 5 6 7 8 9 10 11 12 13 14 15 16 17 18 19 20
Test 1	
Test 2	
Test 3	

There was a limited space on the specimen holder for the samples. Therefore, all of the samples chosen for this project could not be tested for both the corrosion rate and the stress corrosion experiments. Each experiment consisted of the same amount of specimens. The list of materials for each experiment can bee seen in Table 5.5.

Table 5.5: Material selection for each experiment. Shows amount and type of specimens selected.

		Corrosion specimens	
Type	Material	Coupon	U-bend
Carbon Steel	S235 (St.37)	4	
Stainless steel	304L		2
	316L	4	2
	SAF 2205	4	

5.2. Specimen preperation and handling

All specimens were water jet cut into desired size to minimize the risk of getting heat- or stressed affected areas on the edges. They were all marked with identification numbers and then polished in two steps. First step involved polishing with 80 grit SiC abrasive paper and the second with 220 grit, which resembles mill condition of the material and gives similar results as could be expected from the absorption tower material. Specimens were cleaned with water and dried with compressed air between and after these steps. After polishing, specimens were only handled when the operator was wearing latex gloves. Specimens were cleaned with acetone in ultra sonic. After ultra sonic cleaning the sheets were bent to U-shape as shown in Section 5.4. The bending machine was cleaned with acetone before bending. All specimens were photographed before installation into the absorption tower.

Specimens were located onto the specimen holder with 15 mm spacing between them according to standard ASTM G4-01 (2001). POM plastic was used to isolate the specimens from each other as well as to isolate the bolt, washers and nut from the U-bent testing material. Figure 5.4 shows the final look of mounted test specimens onto the specimen holder.

Figure 5.4: Mounted specimens onto the specimen holder before installation.

After testing, all specimens were handled by the operator wearing latex gloves. Specimens

were photographed and put in a desiccator box. Some coupon samples were weighed and cleaned for weight loss measurement. Weight loss samples were cleaned by dipping them into a solution to dissolve the corrosion products and scaling materials from the surface. The Carbon steel S235 was dipped into an aqueous solution of HCL and hexamethylene tetramine at room temperature while the stainless steels were dipped into aqueous solution of NaOH and Zinc while boiling, as explained in standard ASTM G1-90 (1999). Three coupon specimens, one of each type, 316L, S235 and Duplex 2205 were cross-sectioned in selected areas and molded into conductive polymer, bakelite. The molding procedure consist of heating the polymer and applying pressure in a special casing machine. The molded specimens were polished in steps through a series of different abrasive papers. specifically in the order of 80-220-500-1200 and 2400 grit SiC papers. Same technique was applied here as before testing, between and after these steps the molded specimens were cleaned with water and dried with compressed air as soon as possible. After the last step, all molded specimens were inserted to a desiccator box for storage and then analysed with SEM and XEDS.

5.3. Corrosion coupon samples

Three different materials were chosen for corrosion rate measurements for comparison to 316L in the high H_2S concentrated area, respectively S235, 304L and Duplex 2205. Coupons were water jet cut from 3 mm plates with diameter 45 mm and 11 mm hole in the middle.

This experiment was carried out on site at Hellisheiði power plant inside the absorption tower. Three experiments were done where each test contained twelve metal coupons, four of each material type mentioned earlier. Then three samples of each material were cleaned and weigh measured to estimate corrosion rates. The corrosion rate and averages were calculated as instructed in standard ASTM G1-90 (1999). One specimen of each material was cut and molded into bakelite for further examination in SEM.

5.4. U-bent samples

Austenitic stainless steel 304L was chosen to be compared to 316L for SCC. In order to study the SCC of 304L and 316L steels in high H_2S concentrated environment, U-bend test method was used, according to standard ASTM G30-97 (2009). Test specimens of the size 90x15x3 were water jet cut from 304L and 316L plates with the longitudinal direction parallel to the rolling direction of the steel plate. All specimens were bent around a predetermined radius of 15 mm with a custom made U-bend machine capable of providing single stage stressing as can be seen in Figures 5.5a to 5.5c. Grade A4 stainless steel bolts and nuts were used to complete the bending and maintain the stress generated.

The bolts and nuts were were insulated from the sample with POM plastic. All samples were bent to 20% strain.

(a) 1   *(b) 2*   *(c) 3*

Figure 5.5: Bending technique used in this experiment.

Testing was carried out on site in the absorption tower located at Hellisheiði power plant and the samples were fixed on a specimen holder and put into an environment discussed in section 5.1. Specimens were examined on the outer surface stressed area with optical light microscope to verify the absence of cracks before testing in the tower.

6. Results

6.1. 4 week testing with variance in performance

The first test in the air cleaning station at Hellisheiði power plant was a 4 week testing. When samples were inserted into the absorption tower the station was not running due to a failure in the system, however, 15 minutes after insertion the tower began to run again and stopped twice in the following weeks to come. Total stoppage time of the station was 8 hours and 15 minutes during those 4 weeks, another factor to consider is that the station was running at lower production capability than usual during the christmas holidays, for nearly 337 hours. Table 6.1 gives an overview of the performance of the absorption tower during those 4 weeks.

Table 6.1: Overview of Air cleaning station during first 4 weeks of experiment [hours].

Total	Running	Stop	Low production capability
723.05	714.80	8.25	336.80

6.1.1. Coupons - Results

Visual Inspection

Visual inspection can be divided into two phases. Firstly, visual inspection where corrosion and scaling products were on the surface and the second phase where visual inspection was performed after chemical cleaning.

(a) S235 carbon steel   (b) SS 316L   (c) Duplex 2205
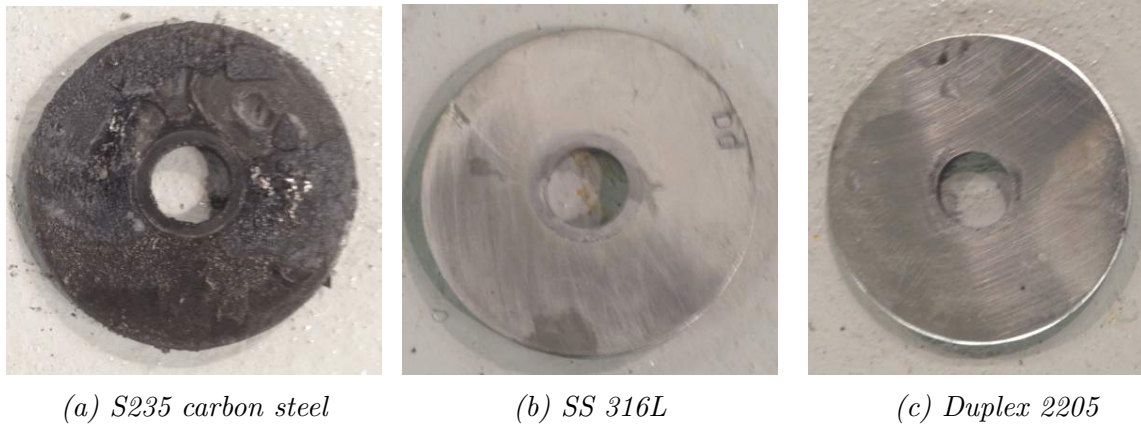
Figure 6.1: Coupons after they were collected from the absorption tower.

Visual inspection on carbon steel S235 showed a layer of dark corrosion products on the surface. The layer was hard, loose and fragile, specially after it had dried up, meaning that the corrosion products could easily fall of the sample. One carbon steel sample showed significant material loss. Figure 6.2 shows the difference on the carbon steel samples after chemical cleaning, it is clear that the lower sample was more corroded than the other.

(a)   (b)
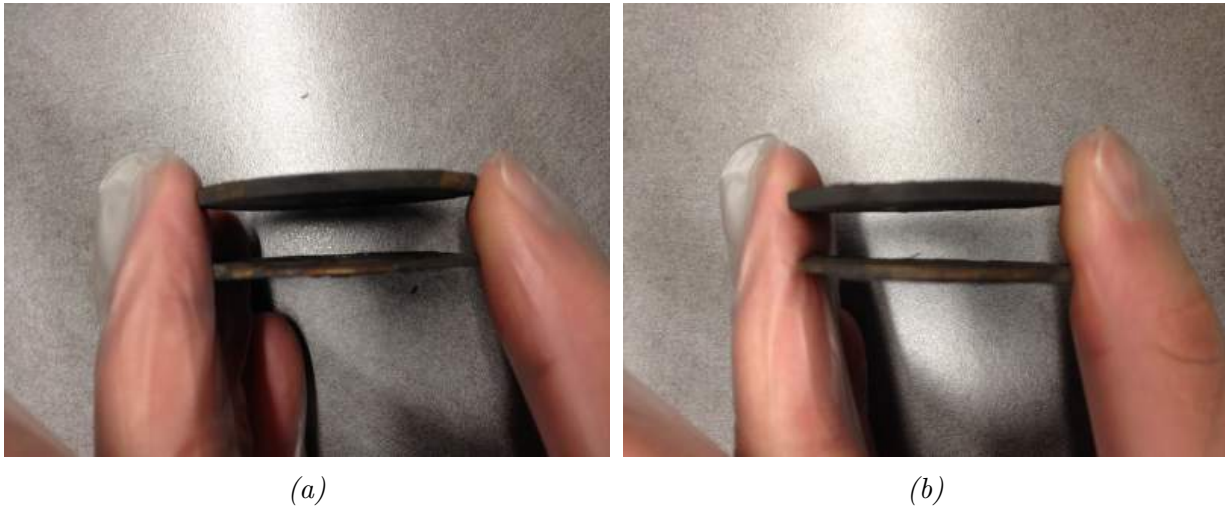
Figure 6.2: S235 Carbon steel. Thickness difference of the samples after a 4 week test.

Visual inspection on stainless steels 316L and Duplex 2205 showed a thin scale which was loose on the surface and could be easily cleaned off. The scaling was not uniform over the surface. No signs of corroded areas could be found and scratches from polishing to 220 grit were still visible.

Figure 6.3 shows the samples after chemical cleaning. From Figure 6.3a it can be seen how cracks have formed on the carbon steel sample S235 and a blistered surface, resembling

Hydrogen Induced Cracking (HIC) damages. The stainless steels, Figures 6.3b and 6.3c, were scale free and still showed no signs of corrosion. Further examination with the scanning electron microscope (SEM) and X-ray energy dispersive spectroscope (XEDS) was used for analysing and to verify the absence of cracks and corrosion damages in the stainless steels as well as investigate the corrosion on the carbon steel. These results along with corrosion rate results are shown in the following sections.

| *(a) S235 carbon steel* | *(b) SS 316L* | *(c) Duplex 2205* |

Figure 6.3: Coupons after they were chemically cleaned.

Corrosion rate

Corrosion rate was calculated with weight loss method. Table 6.2 shows the results for tested materials. The Table is generated with data from Table B.1 in Appendix which shows the overall corrosion rate results for this thesis.

Table 6.2: Corrosion Rate results from first 4 week experiment.

Material Type	Corrosion Rate [mm/yr]	Average Corrosion Rate [mm/yr]
Carbon Steel S235	2.46 7.72 2.57	4.25
Austenitic Steel 316L	$-1\times^{-5}$ $-3.4\times^{-4}$ $-3.3\times^{-4}$	0
Duplex Steel 2205	$7.6\times^{-4}$ $-9.8\times^{-4}$ $-2.2\times^{-4}$	0

Table shows 6.2 that Carbon steel S235 is corroding $2.4 - 7.7$ mm/yr in this environ-

ment while 316L and Duplex 2205 are showing outstanding performance with nearly no corrosion rate measured.

Examination and analysis

S235 coupon
For chemical composition analysis on the corrosion and scaling layer as well as microstructural examination, SEM and XEDS were used. SEM and XEDS was used on two out of three coupons to analyze the corrosion products on the surface before they where cleaned for corrosion measurement or cut and molded into bakelite. The corrosion product on the highly corroded sample was compared to the normal corroded one. Examination on the corroded surface layer was carried out and the SEM showed that the corrosion layer on the carbon steel S235 was of two kinds, the inner surface of the layer is more porous than the dense outer surface, this is visible in Figure 6.4.
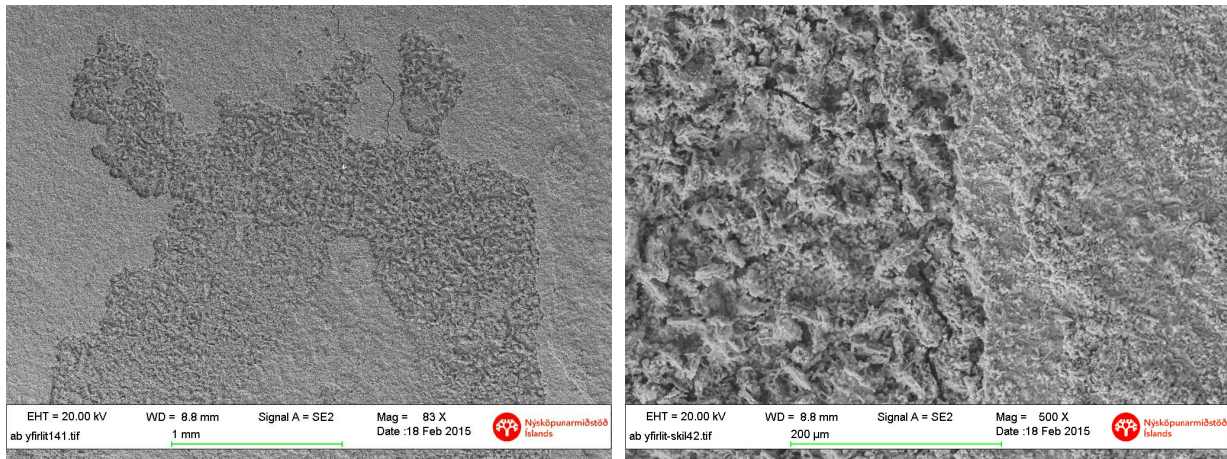
(a) S235 carbon steel	*(b) S235 Carbon steel*

Figure 6.4: SEM images of the surface of carbon steel S235.

Figure 6.5a shows the areas tested for chemical analysis on S235 carbon steels. The sample on Figure 6.5a, which is the highly corroded sample and the sample on Figure 6.5b which represents a regular corroded sample. Figure 6.6 and Table 6.3 show results for these selected parts of the samples.
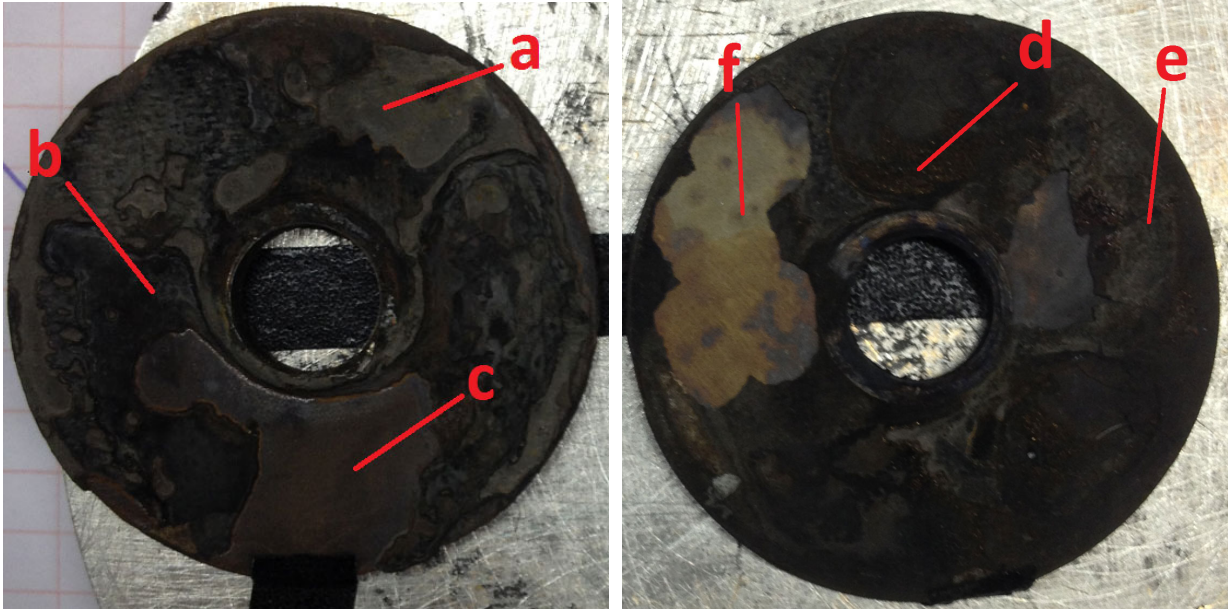
(a) sample ab

(b) sample ad

Figure 6.5: Locations on the surface of carbon steel S235 samples where XEDS analysis were performed, highly corroded sample (a) and normal corroded sample (b).

Figure 6.6: SEM images of the surface of carbon steel S235 where the chemical composition analysis were performed, the area indicated with a purple box.

Table 6.3: XEDS results of the surface of carbon steel S235 specimens shown in Figure 6.5 [Weight%].

Location	C	O	S	Mn	Fe
a	1.3	3.5	48.9		46.3
b		23.7	19.7	1.0	55.6
c		33.3	3.1	0.5	63.1
d		15.4	25.0		59.6
e	1.6	14.5	47.0	0.4	36.5
f	0.6	9.3	2.1	0.7	87.3

XEDS results for the two carbon steels S235 from Table 6.3 gave the results that the corrosion layer is a mixture of iron sulfides and iron oxides. Which later was supported by results from cross-sectioned specimens that was analyzed. No difference in corrosion products could be found for these two samples.

The sample from Figure 6.5b was cross-sectioned and examined further. Figure 6.7 shows an overview of the surface corrosion found in the carbon steel and the location selected

for chemical composition analysis. Chemical composition results are shown in Table 6.4.
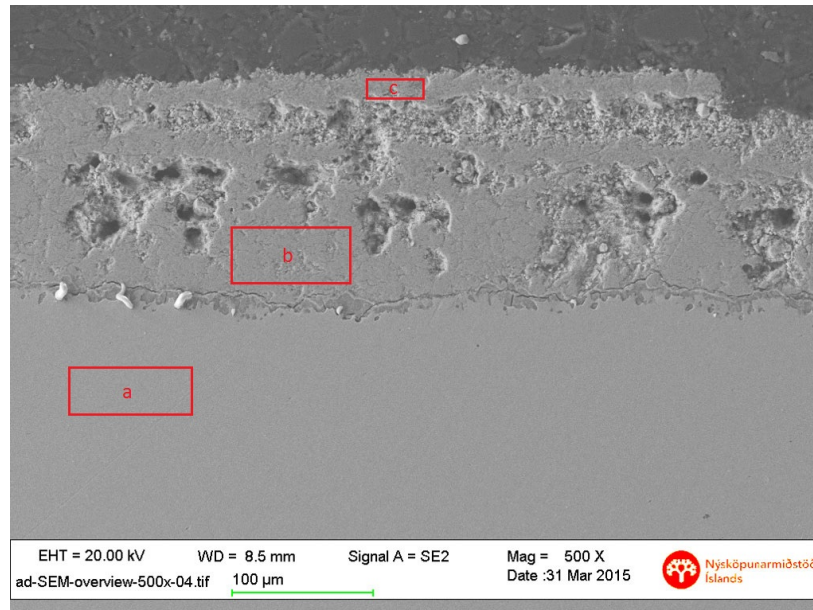
Figure 6.7: SEM image of the cross-sectioned carbon steel S235 where the chemical composition analysis were performed, the area indicated with a red box.

Table 6.4: XEDS results of the cross-sectioned carbon steel S235 specimen from Figure 6.7 [Weight%].

Location	O	Si	S	Mn	Fe
a (bulk)				0.6	99.4
b (inner layer)	13.5	0.3	25.2	0.3	60.7
c (outer layer)	15.8	0.3	25.3	0.8	57.8

Table 6.4 shows that the corrosion layer mostly consists of oxygen (O), sulfur (S) and iron (Fe). From the analysis it can be estimated that the corrosion layer is mostly iron sulfides and iron oxides. It can also be estimated that the outer corrosion layer has more of iron oxides than the inner corrosion layer.

Figure 6.8 shows the surface corrosion layer as well as some cracks in the middle of the sample. From the appearances and the environment this is believed to be caused by HIC. The arrow on Figure 6.8a shows the crack where XEDS analysis were performed. Chemical composition results are shown in Table 6.5.
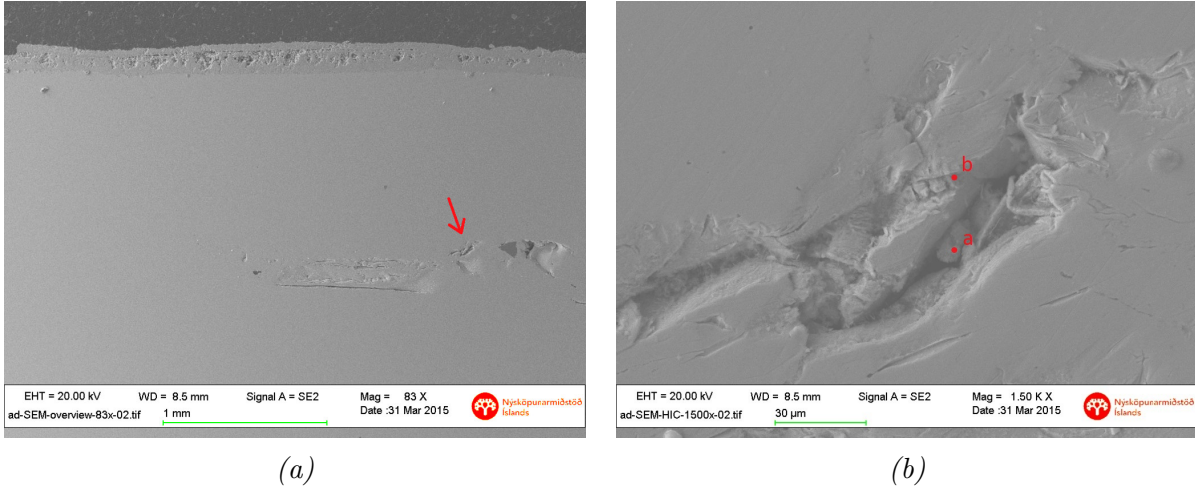
Figure 6.8: SEM image of carbon steel S235, showing an overview of the HIC on the sample. Red arrow points to the HIC damages where XEDS analysis were performed. The areas indicated with a red point on Figure 6.8b.

Table 6.5: XEDS results of the cross-sectioned carbon steel S235 specimen from Figure 6.8 [Weight%].

Location	O	Si	Mn	Fe
a	5.5	0.5		94.0
b	16.7	1.9	0.7	80.7

Table 6.5 shows the oxygen is present in the HIC damages. Possible iron oxides, a corrosion product from oxygen ingress into the HIC crack during testing.

After chemical cleaning of the selected S235 carbon steels, blisters were obvious on the surface of the samples as previously discussed. Figure 6.9 shows the surface of a selected carbon steel S235 that showed the most damages in three different locations. Figure 6.9b shows the blisters on the surface and cracks that have initiated near the blisters ends. These blisters are considered to occur when the hydrogen (H) diffuses into the BCC structure of the carbon steel and combines with another hydrogen (H) and forms H_2. The formation of H_2 creates internal pressure inside the carbon steel and because of ductility blisters are formed on the surface as well as the cracks in the middle of the metals cross-section.

(a) S235	(b) S235	(c) S235

Figure 6.9: Microscopic images of Carbon steel S235 surface after chemical cleaning.

316L coupon

Similar to the carbon steel S235 the surface of the stainless steels specimens was examined. SEM and XEDS was used to determine the corrosion or scaling layer. Figure 6.10 shows an overview of the scaling found on the surface of stainless steel 316L along with the locations chosen for chemical composition analysis of the scale.

(a) 316L	(b) 316L
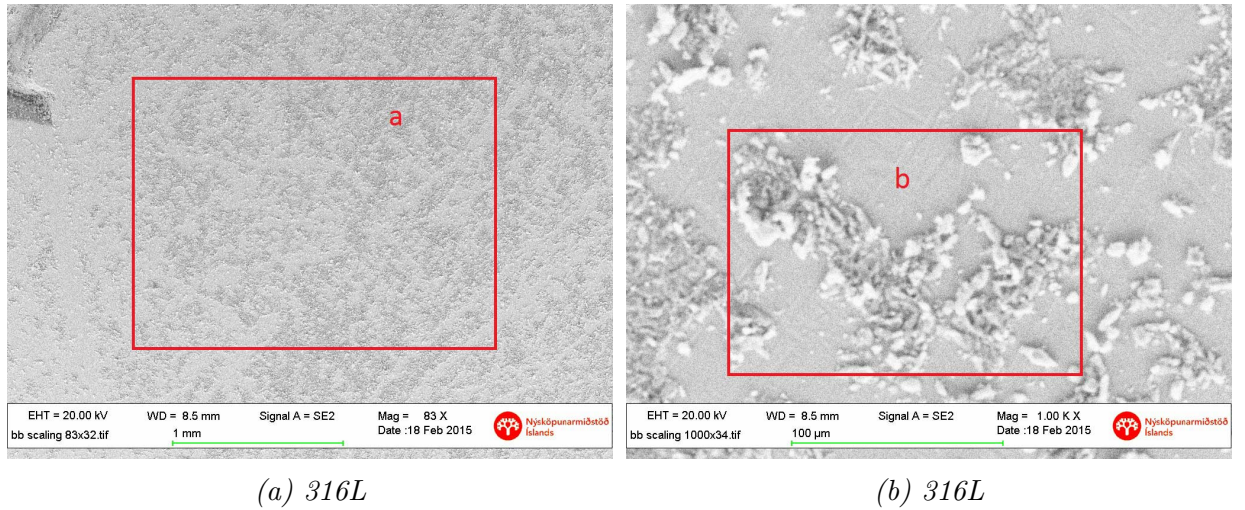
Figure 6.10: SEM images of the surface of austenitic stainless steel 316L where the chemical composition analysis were performed, the areas indicated with a red box.

Figure 6.10 shows that the scaling does not cover the surface completely. XEDS analysis were made on the surface. Chemical compositions of the surface of 316L is shown in Table 6.6.

6. Results

Table 6.6: *XEDS results for the surface analysis of 316L from Figure 6.10 [Weight%].*

Location	Si	S	Cr	Mn	Fe	Ni
a	0.4	37.5	12.0	0.8	43.2	6.1
b	0.4	30.5	12.6	1.0	49.0	6.5

Table 6.6 shows large amounts of sulfur (S) substances on the surface along with chrome (Cr), iron (Fe) and nickel (Ni). Much of the area analysed is bare metal. Therefore, the scaling was further investigated in Figure 6.11 for the stainless steel 316L. Chemical compositions are listed in Table 6.7.
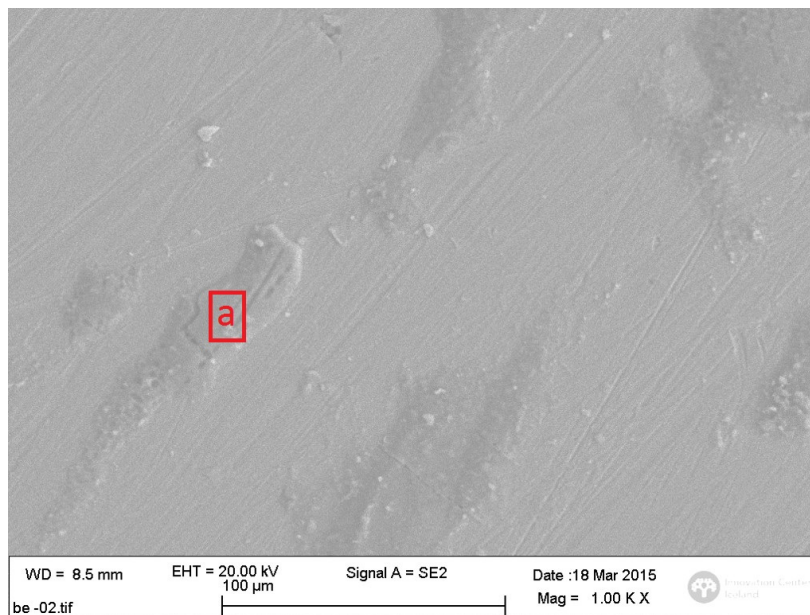
Figure 6.11: *SEM image for more precision XEDS examination on the scaling layer of 316L.*

Table 6.7: *XEDS results for the surface scaling layer of 316L from Figure 6.11 [Weight%].*

Location	S	Cr	Fe	Se
a	96.5	0.5	1.9	1.1

From Table 6.7 it was believed that the scaling layer was pure sulfur (S) due to the oxygen content of the gas inside the absorption tower. It has been reported that for gas phase the reaction of H_2S and oxygen (O) forms pure sulfur along with water (H_2O) (Smith & Craig, 2005).

316L coupon was cross-sectioned and viewed in SEM. During the cutting process of 316L alot of heat generated, smoke rose from the sample and a sulfuric smell. Chemical analysis were conducted on the samples as seen in Figure 6.12. The analysis can be seen in Table 6.8. No scaling on the surface of 316L was detected in SEM. The surface was rough and uneven when examined in SEM. It is believed to be a loose material on the edges after the cutting procedure that have not been removed sufficiently, creating artefacts on the surface that could be interpreted as cracks or pits. However, no cracks or pits were detected on the sample.
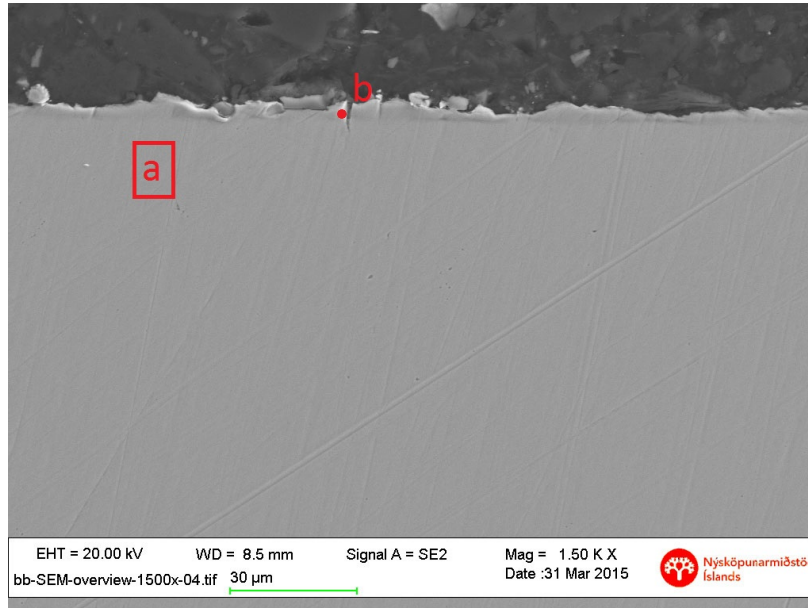
Figure 6.12: Cross-sectioned SEM images of the austenitic stainless steel 316L where the chemical composition analysis were performed, the areas indicated with a red box and a point.

Table 6.8: XEDS analysis of the cross-sectioned austenitic stainless steel 316L from Figure 6.12 [Weight%].

Location	O	Si	Cr	Mn	Fe	Ni	Mo
a (bulk)	1.0	0.5	16.2	1.4	69.5	9.6	2.0
b (artefact)	3.2	1.1	15.3	1.5	67.7	8.8	2.4

The chemical compositions shows that there might be some chromium oxide at the surface and no sulfur (S) or large amount of oxygen (O) was detected which supports the conclusion that it was not a crack but an artefact.

2205 coupon

6. Results

The surface of Duplex stainless steel 2205 was examined with SEM and XEDS. Figure 6.13 shows an overview of the surface scaling and the locations chosen for chemical composition analysis of the scale.

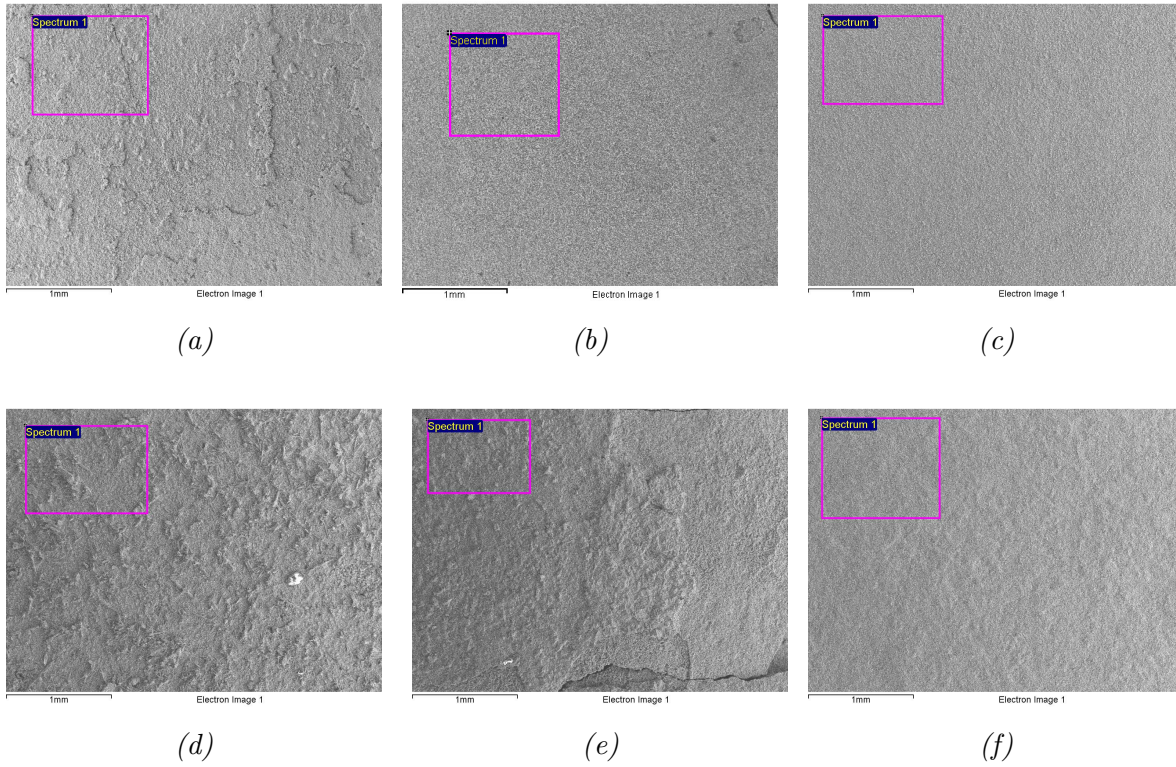(a) Duplex 2205   (b) Duplex 2205
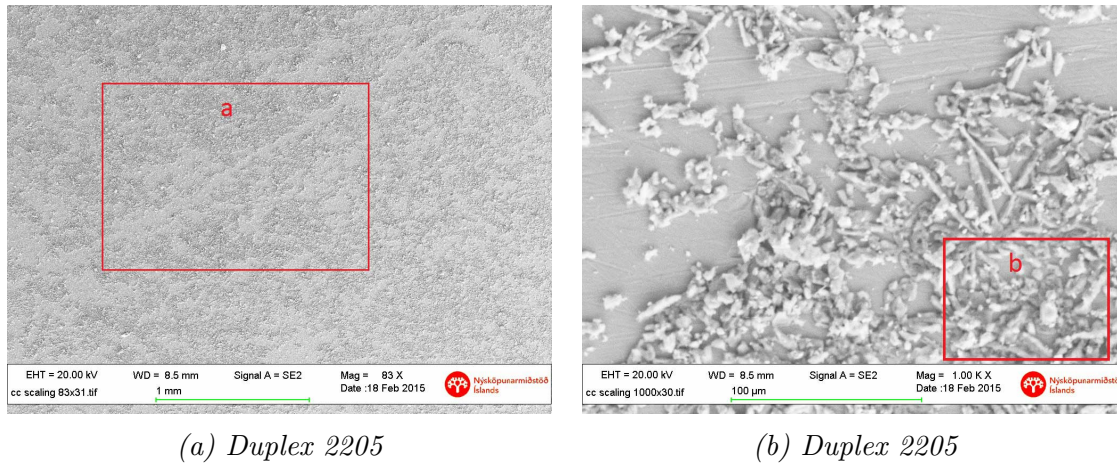
Figure 6.13: SEM images of the surface of duplex stainless steel 2205 where the chemical composition analysis were performed, the area indicated with a red box.

Table 6.9: XEDS results for surface of Duplex 2205 from Figure 6.13[Weight%].

Location	Si	S	Cr	Mn	Fe	Ni
a	0.3	40.8	14.2	1.0	40.9	2.8
b		62.2	8.5	0.5	27.0	1.8

Table 6.9 shows that the layer on the surface mostly consists of sulfur (S), chrome (Cr), iron (Fe) and some amount of nickel (Ni). 2205 is a higher graded material than 316L and therefore, as for 316L, the scaling layer is believed to be pure sulfur.

Duplex 2205 was cross-sectioned and viewed in SEM. Similar as for the 316L, the cutting procedure generated alot of heat that resulted in a smoke and sulfuric smell. Figure 6.14 shows the sample and the locations chosen for chemical composition analysis. It can be seen in Figure 6.14 that the surface is rough and uneven. It is believed to be artefacts from loose material as discussed for 316L. Figure 6.14 and Table 6.10 show locations and chemical composition analysis for Duplex 2205.

Figure 6.14: Cross-sectioned SEM image of duplex stainless steel 2005 where the chemical composition analysis were performed, the areas indicated with a red box and a point.

Table 6.10: XEDS analysis of the cross-sectioned duplex stainless steel 2205 from Figure 6.14 [Weight%].

Location	O	Si	Cr	Mn	Fe	Ni	Mo
a (bulk)	1.0	0.4	21.3	1.5	67.5	5.7	2.6
b (artefact)	1.3	5.3	21.2	1.1	64.3	3.9	2.9

Table 6.10 shows the chemical composition of the artefact. Some silica (Si) is present in the analysis. The silica is believed to come from the SiC papers used for polishing. No corrosion or pits could be found on the sample.

6.1.2. U-bend - Results

Similar to the coupons the heat generated from cutting the sample led to smoke with a sulfur smell coming from the sample.

When 304L was examined in SEM, areas were found that could be interpreted as pits or pit initiations, initiations points for cracking, such as SCC. Figure 6.15 shows the locations where chemical composition analysis were made.

Figure 6.15: Cross-sectioned SEM image of U-bent 304L where the chemical composition analysis were performed, the areas indicated with red boxes.

Table 6.11: XEDS analysis of the cross-sectioned austenitic stainless steel 304L U-bent specimen from Figure 6.15 [Weight%].

Location	O	Si	Cr	Mn	Fe	Ni
a (bulk)	1.0	0.3	17.7	1.8	71.8	7.4
b (pit/artefact)	1.6	35.8	12.0	1.2	45.4	4.0
c (pit/artefact)	2.0	11.0	15.4	1.6	63.7	6.3

Chemical compositions of 304L show that silica is present inside what was believed to be a pit. The compositions collected did not give a clear identification that 304L was experiencing pit initiations and no cracks were found on the sample, therefore Figure 6.15 could be showing an artefact.

Chemical composition analysis for 316L U-bent specimens are shown in Figure 6.16 and Table 6.12.
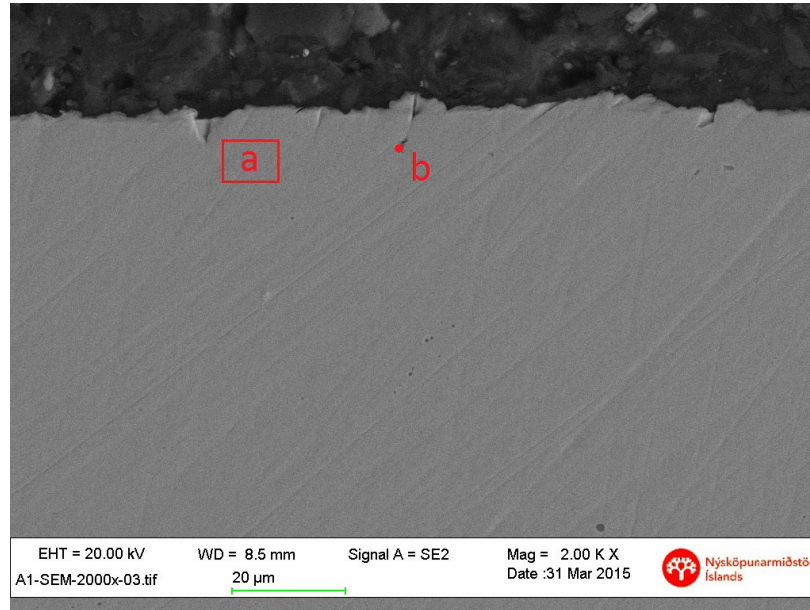
Figure 6.16: Cross-sectioned SEM image of U-bent 316L where the chemical composition analysis were performed, the areas indicated with a red box and point.

Table 6.12: XEDS analysis of the cross-sectioned austenitic stainless steel 316L U-bent specimen from Figure 6.16 [Weight%].

Location	O	Si	Cr	Mn	Fe	Ni	Mo
a (bulk)	1.5	0.5	17.1	1.2	68.1	9.1	2.5
b (crack/artefact)	2.6	6.9	16.0	1.2	63.7	8.0	1.6

Chemical composition analysis for 316L that silica is inside what could be interpreted as a crack. No evidence of cracks or pits were found on the sample. It was believed that chromium oxides had been able to form on the sample as the analysis show.

6.1.3. Summary

From the first 4 week experiment the analysis showed that carbon steel S235 is corroding. The hydrogen (H) inside the absorption tower is believed to diffuse into the BCC structure of the metal and reacts with another hydrogen (H). When the reaction occurs H_2 is formed. The pressure inside the metal becomes high when the reaction occurs and the ductile carbon steel yields and creates blisters on the surface as well as cracks or holes inside the metal. The stainless steels 2205 and 316L show an outstanding performance in the system while pit initiations might occur for 304L stressed sample.

6.2. 4 week testing on regular operation performance

Specimens were inserted into while the station was operating. The specimens were placed in the same position in the absorption tower as in the previous experiment discussed in 6.1. The specimens locations inside the tower were considered to be very similar. The station ran fine until it had to be stopped suddenly to fix some unrelated problem at the power plant. The specimens were withdrawn from the absorption tower after the station had been stopped for over 120 hours. As mentioned earlier these stoppages are not considered to have severe effects on the results but will be documented. Table 6.13 shows an overview of the air cleaning stations performance during testing.

Table 6.13: Overview of Air cleaning station during the second 4 weeks of experiment [hours].

Total	Running	Stop
690.42	565.75	124.68

6.2.1. Coupons - Results

Visual inspection

Similar to the 4 week testing in section 6.1.1 the visual inspection is divided into two phases, before and after cleaning. Figure 6.17 shows the specimens shortly after they were collected from the absorption tower.
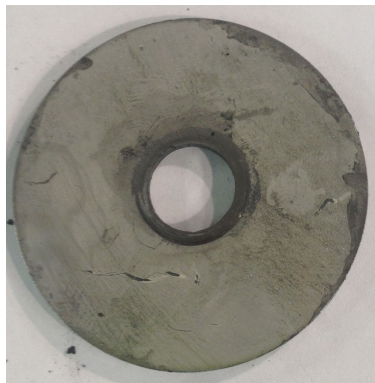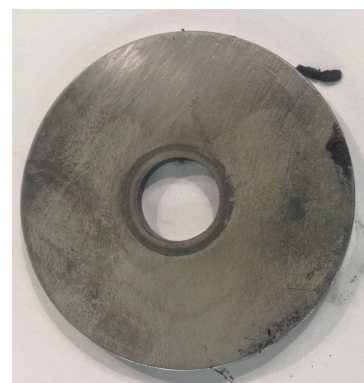
(a) S235 carbon steel   (b) SS 316L   (c) Duplex 2205

Figure 6.17: Coupons after they were collected from the absorption tower.

Corrosion products on carbon steel S235 were dark and loose at the surface. Similar

corrosion damages could be found on one of the S235 sample which was located in the same position as the highly corroded sample from previous test. This extremely corroded specimen can be seen in Figure 6.18 where it is compared to a normal sample which corrodes similar as the others. However, the chemical composition analysis from section 6.1.1 showed that no difference in corrosion products on the surface could be found.
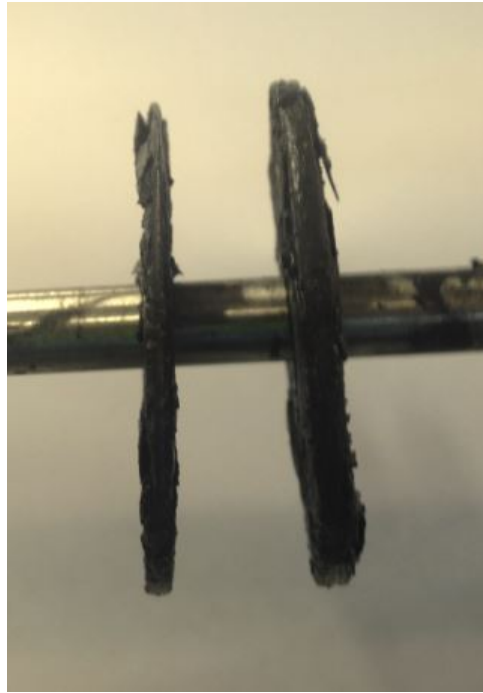
Figure 6.18: Comparison of carbon steel coupons in second 4 week test.

The stainless steels showed similar results as for the first test, a scaling layer that can easily be cleaned off was visible and no sign of corrosion. Prior cleaning it seemed like the same results were expected for both 4 weeks testing, cleaned specimens can be seen in Figure 6.19. However, the corrosion layer on S235 hid an interesting result where it seemed like that surface damages due to HIC on carbon steel S235 were much more severe for this test than the first one.

| (a) S235 carbon steel | (b) SS 316L | (c) SS 2205 |

Figure 6.19: Coupons after they were chemically cleaned.

Figure 6.20 shows an example of difference in corrosion damages where the sample on the right represents this test. Figure 6.20 shows how the sample on the right has more blisters compared to the sample on the left.

| (a) First test | (b) Second test |

Figure 6.20: Comparison on carbon steel S235, 4 week tests.

The stainless steel showed scratches from polishing similar to previous test and no signs of corrosion could be seen which led to a further examination via SEM and XEDS.

Corrosion rate

Corrosion rate was calculated with weight loss method. Table 6.14 shows the result for tested materials. The Table is generated with data from Table B.1 in Appendix which shows the overall corrosion rate results for this thesis. Carbon steel S235 showed a poor performance under these conditions while both of the stainless steels showed outstanding performance with almost no corrosion rate measured.

Table 6.14: Corrosion Rate results from the second 4 week experiment.

Material Type	Corrosion Rate [mm/yr]	Average Corrosion Rate [mm/yr]
Carbon Steel S235	2.21 7.59 2.58	4.13
Stainless Steel 316L	$2.3\times^{-4}$ $2.0\times^{-4}$ $2.1\times^{-4}$	$2.13\times^{-4}$
Duplex Steel 2205	$-1.4\times^{-4}$ $7.0\times^{-4}$ $3.8\times^{-4}$	$3.6\times^{-4}$

Examination and analysis

S235 coupon
Carbon steel S235 was again lacking in performance, showing thick corrosion layer and clear signs of hydrogen induced cracking (HIC). The corrosion products were examined and Figure 6.21 shows the corrosion and the locations for chemical composition analysis. The analysis are listed in Table 6.15
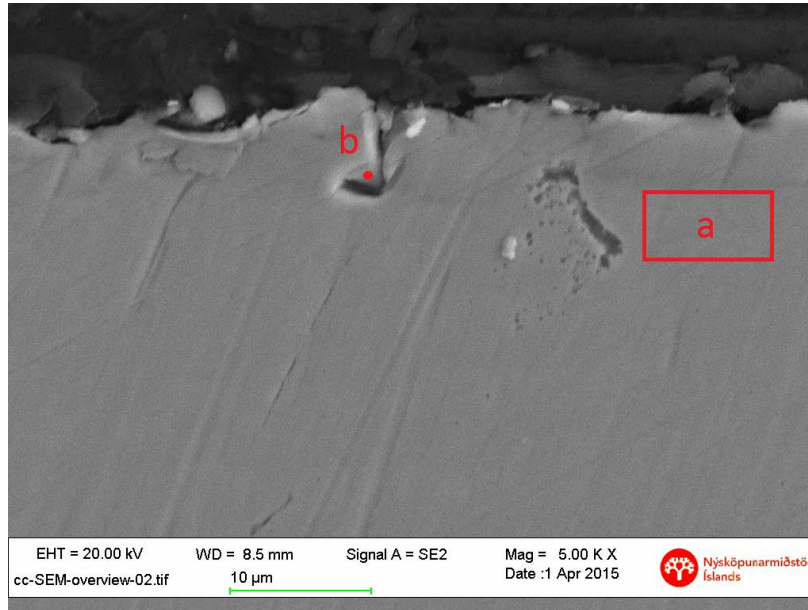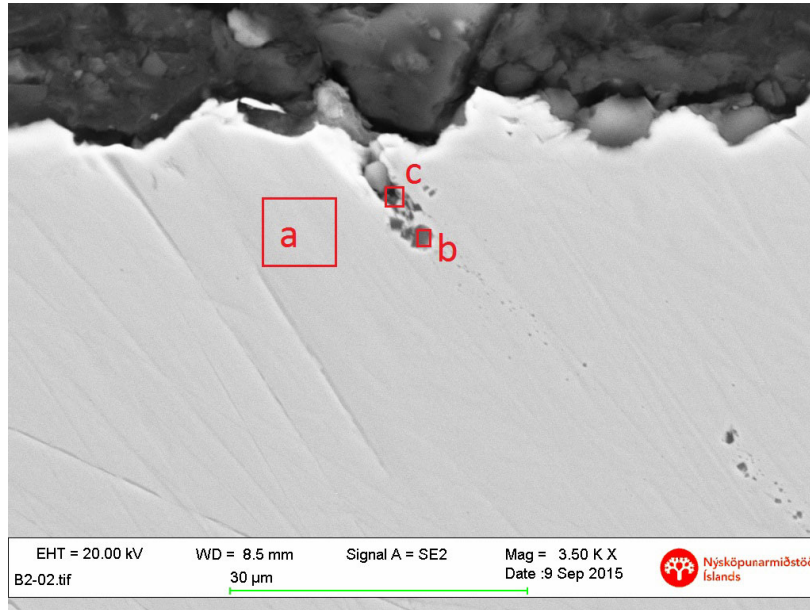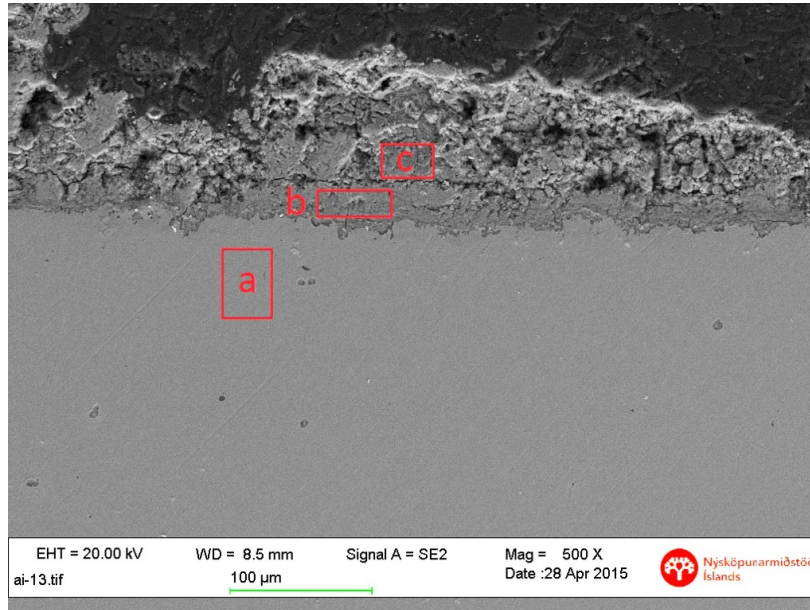
Figure 6.21: Cross-sectioned SEM image of carbon steel S235 coupon where the chemical composition analysis were performed, the areas indicated with a red box.

Table 6.15: XEDS results of the cross-sectioned S235 specimen from Figure 6.21 [Weight%].

Location	O	Si	S	Mn	Fe
a (bulk)				0.8	99.2
b (inner scale)	27.1	1.0	7.9	0.5	63.5
c (outer scale)	22.6	1.0	17.6		58.8

Table 6.15 shows that the corrosion products were iron sulfides and iron oxides. HIC damages on the sample were examined and are shown in Figure 6.22 and the analysis are listed in Table 6.16.

(a)

(b)
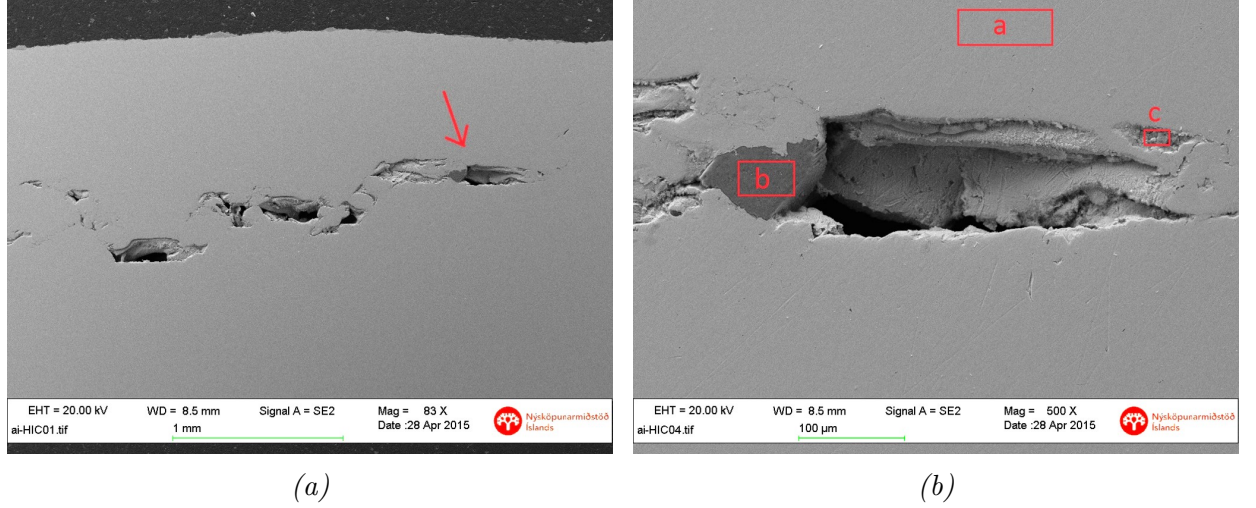
Figure 6.22: SEM images of the cross-sectioned carbon steel S235 where the chemical composition analysis were performed on the HIC damages, the area indicated with a red box.

Table 6.16: XEDS results of the cross-sectioned S235 specimen from Figure Figure 6.22 [Weight%].

Location	O	Si	S	Fe
a (bulk)		0.8		99.2
b	7.3	90.0		2.7
c	32.6	3.2		64.2

Table 6.16 shows that the dark material in the hole is silica (Si). The silica is believed to come from the polishing where SiC abrasive papers used. Some oxygen in present near the holes. Possible iron oxides, a corrosion product from oxygen ingress into the HIC crack during testing. After cleaning of the carbon steel S235 samples, the surface and blisters were found on the surface and photographed with an optical light microscope. Figure 6.23 shows the surface of the carbon steel in three different locations, showing the damages on the surface.

(a) S235	(b) S235	(c) S235
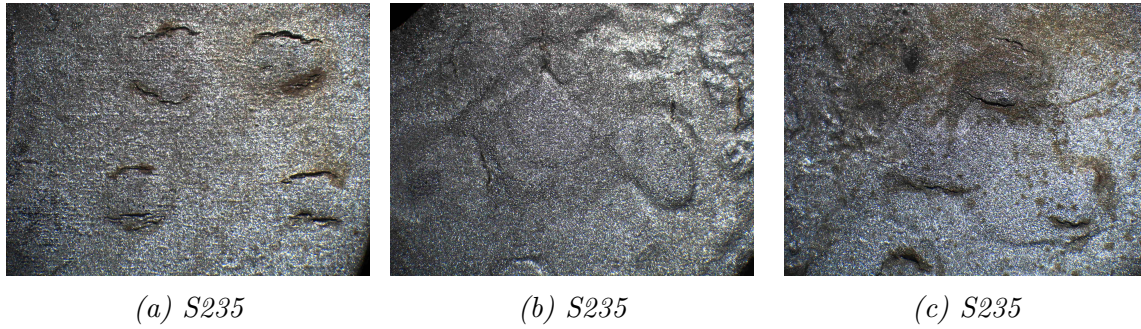
Figure 6.23: Microscopic images of Carbon steel S235 surface after cleaning.

316L coupon

The stainless steel 316L showed no signs of corrosion damages as can be seen from the following SEM and XEDS analysis below. Heat was generated while cutting the sample and a sulfuric smell rose from the smoke. It was believed that the thin scale on the surface of the specimen could have evaporated. Figure 6.24 shows the locations for chemical composition analysis. The analysis are listed in Table 6.17
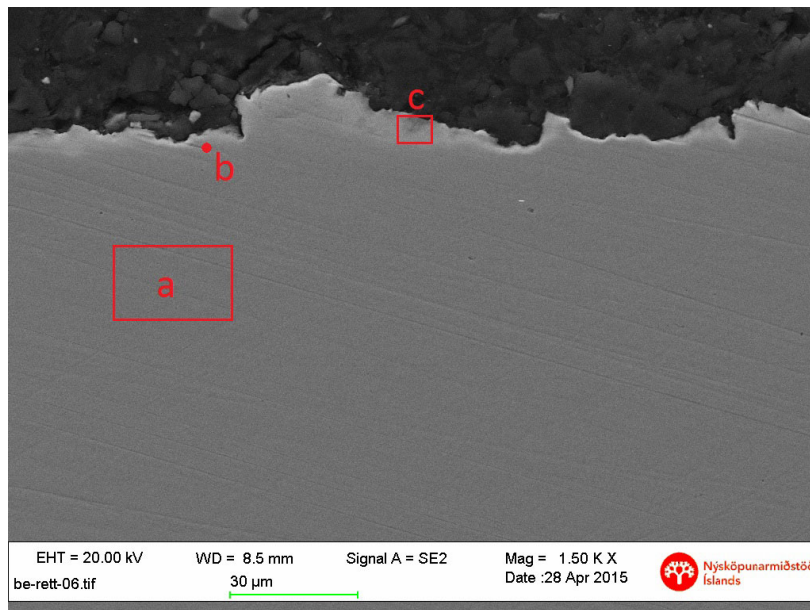
Figure 6.24: Cross-sectioned SEM image of stainless steel 316 coupon where the chemical composition analysis were performed, the areas indicated with a red box and point.

Table 6.17: XEDS analysis of the cross-sectioned austenitic stainless steel 316L from Figure 6.24 [Weight%].

Location	C	O	Si	Cr	Mn	Fe	Ni	Mo
a (bulk)			0.6	17.8	1.4	68.3	9.9	2.0
b (crack/artefact)	2.2	7.0	1.9	14.4	1.3	62.8	8.7	2.0
c (surface)	61.8	5.7	0.4	5.5	0.5	22.1	3.4	0.6

Table 6.17 shows that chromium oxides might be on the surface and the high carbon content found was believed to come from the bakelite. What was believed to be a crack or an artefact shows an oxygen content that might be chromium oxides. No evidence of corrosion products were found on the sample during inspection.

2205 coupon

XEDS analysis were made for Duplex 2205. The uneven and rough surface of the specimens are believed to be from the cutting procedure, where loose material has not been removed sufficiently and showing artefacts that could be interpret as pits or cracks. Figure 6.25 shows selected locations for XEDS analysis and Table 6.18 shows chemical results on selected locations.
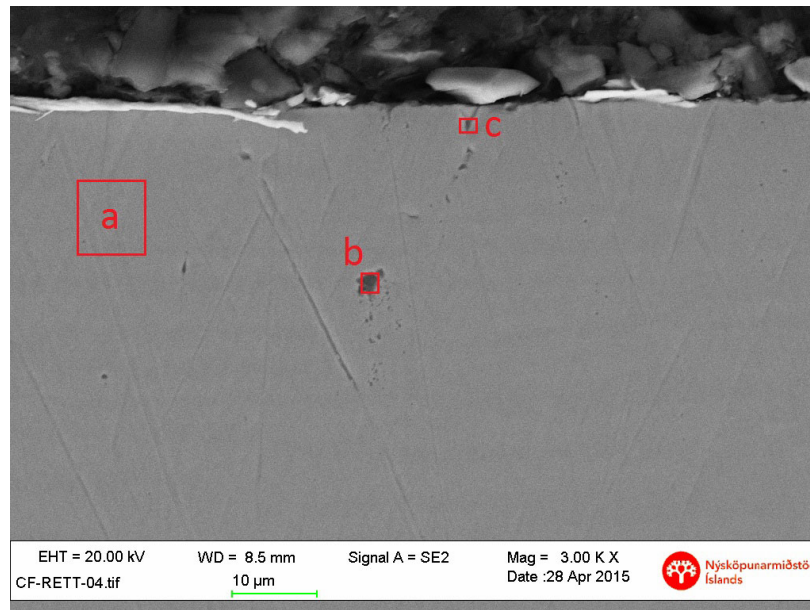
Figure 6.25: Cross-sectioned SEM image of duplex stainless steel 2205 coupon where the chemical composition analysis were performed, the areas indicated with red boxes and point.

Table 6.18: XEDS analysis of the cross-sectioned duplex stainless steel 2205 from Figure 6.25 [Weight%].

Location	C	O	Si	Cr	Mn	Fe	Ni	Mo
a (bulk)		1.3	0.4	21.0	1.3	67.4	5.6	3.0
b (black dot)	5.3	1.1	48.6	11.9	0.8	29.5	1.7	1.1
c (crack)	1.6		3.3	22.4	1.1	64.3	4.2	3.1

Table 6.18 shows that for location b there is high silica amount and some carbon (C) content, suggesting that there might have been a scratch of some kind that might have been filled up with silica and bakelite from polishing. Anaysis show that that was believed to be a crack or a pit initiation in location c is possibly an artefact or a flaw in the material. No traces of corrosion products or cracks were found on the sample.

6.2.2. U-bend - Results

Similar to previous test, alot of heat was generated during cutting and preparing of the specimens for SEM. When examined in SEM, the stainless steel 304L showed cracks on the surface. Figure 6.26 shows the crack and chemical composition analysis are in Table 6.19

(a)   *(b)*
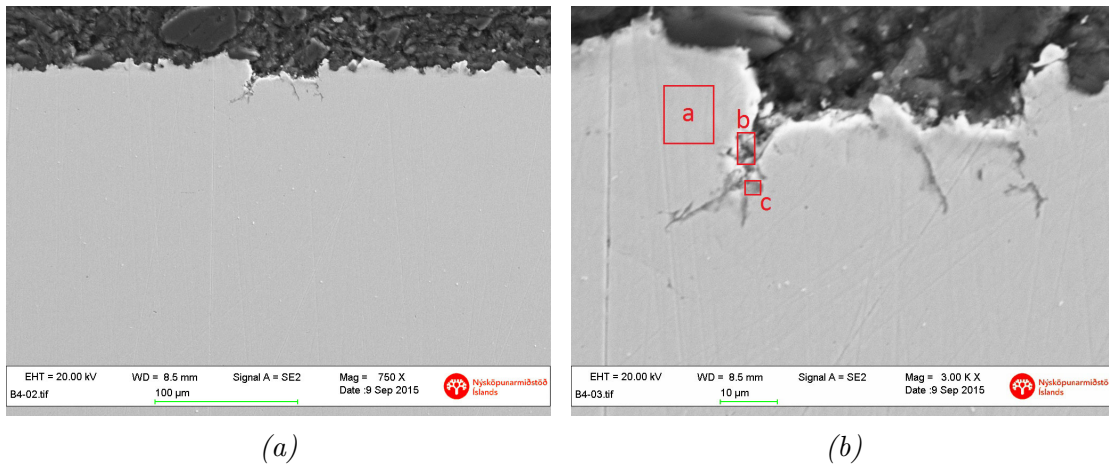
Figure 6.26: SEM images of the cross-sectioned 304L U-bent sample where the chemical composition analysis were performed, the area indicated with red boxes.

Table 6.19 shows that the crack is rich with sulfur (S), oxygen (O) and nickel (Ni).

Results for 316L U-bent specimens are shown in Figure 6.27 and Table 6.20.

Table 6.19: XEDS analysis of the cross-sectioned austenitic stainless steel 304L U-bent specimen from Figure 6.26 [Weight%].

Location	C	O	S	Na	Cr	Mn	Fe	Ni	Cu
a (bulk)			0.2		17.5	1.9	72.5	7.9	
b (pit)	5.4	17.1	27.8	2.3	13.7	0.3	7.2	24.6	1.6
c (crack)	1.5	19.1	22.4	2.3	15.4	0.6	16.0	21.5	1.2
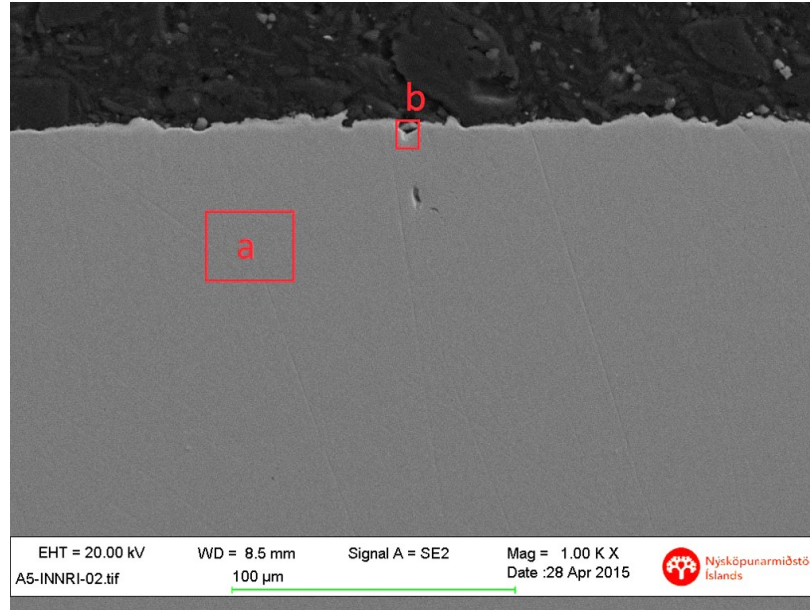
Figure 6.27: SEM image of the cross-sectioned U-bent 316L sample where the chemical composition analysis were performed, the areas indicated with a red box.

Table 6.20: XEDS analysis of the cross-sectioned austenitic stainless steel 316L U-bent sample from Figure 6.27 [Weight%].

Location	C	Si	Cr	Mn	Fe	Ni
a (bulk)		0.4	19.2	1.9	70.3	8.2
b (artefact)	20.8	29.5	10.6	1.1	34.6	3.4

Table 6.20 shows that high amounts of carbon (C) and silica (Si) were present, suggesting that the area selected in the picture is most likely an artefact. Only artefacts such as this on the picture were found, and no pits or cracks were present during inspection.

6.2.3. Summary

From the second 4 week experiment the analysis showed that carbon steel S235 is corroding similar as for the previous test. The HIC damages from hydrogen diffusion into the carbon steel S234 were believed to be more severe than for the first test. The carbon steel S235 sample showed more blisters on the surface in visual inspection. Crack was seen on the 304L sample showing high amounts of sulfur (S), oxygen (O) and nickel (Ni) in the crack. The corrosion rate results show that the stainless steels 316L and 2205 had an outstanding performance in the tower.

6.3. 12 week testing

Specimens were inserted while the station was operating. Specimen location in the tower was similar to those found in previous experiments from Sections 6.1 and 6.2. According to data from the station it stopped two times for several days combined, the stoppages are not considered to have significant effects on the results but will be documented. In the end of this test ON was conducting an stress experiment where the condensed water was being pumped in at approximately 60 l/s, compared to the 34-36 l/s usually pumped through the tower. No extra gas was injected through the tower on that period. However, ON took samples on the gas going to the absorption tower during their stress experiment where the oxygen levels showed up to 5.4 % of total volume of the gas. This is recorded in Appendix A in Table A.1 on May 6th (6.5.2015). For how long this lasted is not known, on May 6th the station started running again after a 4 days stoppage.

Table 6.21: Overview of Air cleaning station during first 4 weeks of experiment [hours].

Total	Running	Stop	System under stress testing
2035.92	1844.58	191.34	2.00

6.3.1. Coupon - Results

Visual inspection

Similar to previous 4 week tests, visual inspection was divided into two phases, before and after cleaning. Specimens shortly after they were collected from the absorption tower can be seen in Figure 6.28

| (a) S235 carbon steel | (b) SS 316L | (c) SS 2205 |

Figure 6.28: Coupons after they were collected from the absorption tower.

For both the 4 weeks tests, one carbon steel coupon of total four was clearly more corroded than the others. However, for this test two coupons were clearly more corroded. Comparison of all the carbon steel coupons in this experiment can be seen in Figure 6.29, the figure shows a clear difference in thickness of the samples. The two coupons that were clearly more corroded showed dark and thin corrosion products on the surface while the two remaining coupons were similar to the once from previous experiments. That is, a thick dark layer which is loose at the surface and can easily fall off. Different from the first two 4 week experiments the highly corroded coupons are located in a different spot at the specimen holder, which means that it has a different location inside the absorption tower. Visual inspection on stainless steels shows similar scaling layer as in previous experiments, a thin layer that can easily be wiped off.

Figure 6.29: Comparison on carbon steel coupons for the 12 week testing, showing difference in thickness due to corrosion.

6. Results

Specimens after cleaning can be seen in Figure 6.30. The scratches from polishing prior to the test were visible on the stainless steels and no signs of material degradation could be detected. Figure 6.31 shows the difference in corrosion for the carbon steel S235 coupons for this test, the Figure shows the samples with and without corrosion products on the surface.

(a) S235 carbon steel *(b) SS 316L* *(c) SS 2205*

Figure 6.30: Coupons after they were chemically cleaned.

(a) *(b)* *(c)*

(d) *(e)* *(f)*

Figure 6.31: Comparison on S235 coupons before and after cleaning.

Cleaned specimens for weight loss measurement showed similar corrosion damages as found in previous experiments. The three carbon steel coupons used for weight loss measurement were all different in terms of thickness. Their thickness can be seen in Figure 6.29, coupons used were the first three from the left.

Corrosion rate

Table 6.22 shows the corrosion rate result for tested materials. The Table is generated with data from Table B.1 in Appendix which shows the overall corrosion rate results for this thesis. Stainless steels show outstanding performance under these circumstances while carbon steel S235 shows a poor performance, however, carbon steel S235 shows a better corrosion rate for the 12 week experiment than for the previous 4 week experiments. That could be because of the corrosion products on the surface protecting the bare metal and slowing down the corrosion rate.

Table 6.22: Corrosion Rate results for the 12 week experiment.

Material Type	Corrosion Rate [mm/yr]	Average Corrosion Rate [mm/yr]
Carbon Steel S235	0.95 4.61 3.40	2.99
Stainless Steel 316L	$-4\times^{-5}$ $1.8\times^{-5}$ $-3\times^{-5}$	0
Duplex Steel 2205	$2.8\times^{-4}$ $-2.4\times^{-4}$ $5.0\times^{-4}$	0

Examination and analysis

S235 coupon
Figure 6.32 shows the surface of the S235 sample.

(a) S235 carbon steel
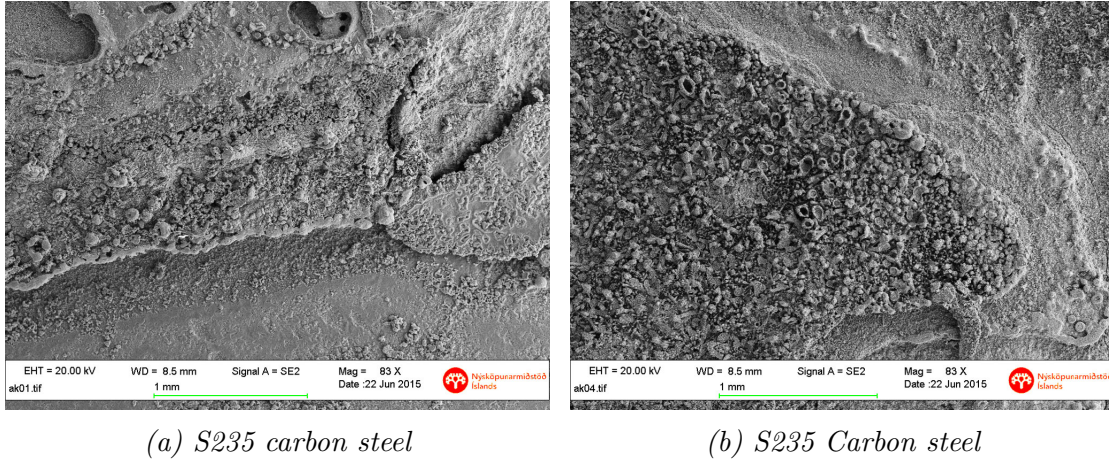
(b) S235 Carbon steel

Figure 6.32: SEM images of the surface of carbon steel S235 after 12 weeks testing.

Chemical composition via XEDS was performed with greater depth than in previous test from Section 6.1.1. Figure 6.33 and Table 6.23 show the locations where chemical composition analysis were performed. The analysis of the microstructure of the corrosion layer was believed to give more accurate results on the corrosion layer composition than in previous tests.

(a)

(b)
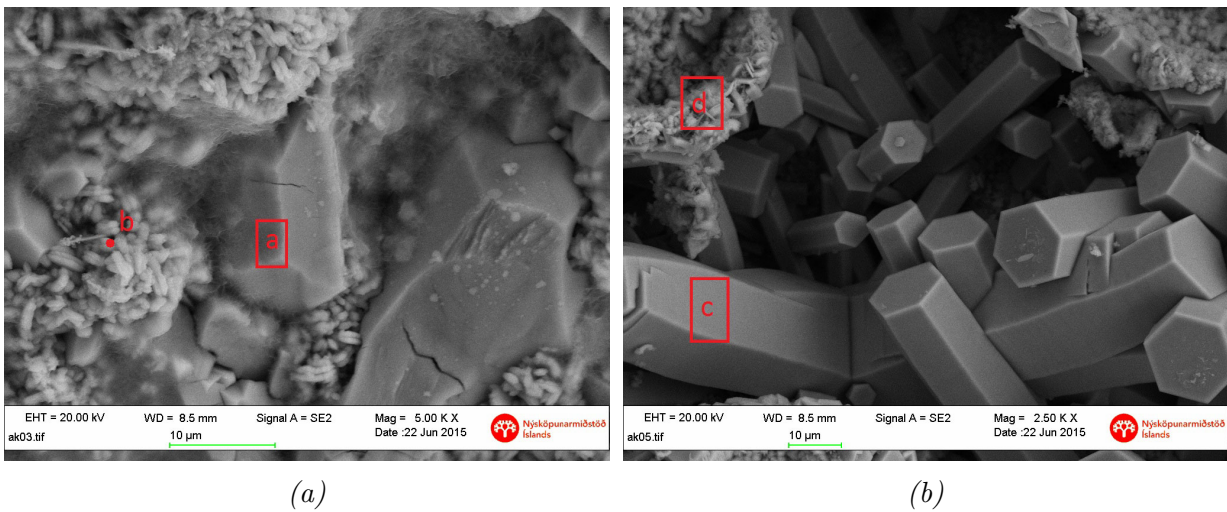
Figure 6.33: SEM images of the corrosion products on the surface of carbon steel S235 after 12 weeks testing. Chemical composition analysis were performed, the areas indicated with red boxes and a point.

Table 6.23: XEDS results of the surface of carbon steel S235 specimen after 12 week testing from Figure 6.33 [Weight%].

Location	O	S	Mn	Fe
a	7.4	33.4		59.2
b	18.0	29.3	1.3	51.4
c	5.6	37.1		57.3
d	5.6	14.9		79.5

Table 6.23 shows the microstructure of the iron sulfides, location a and c. Location b and d might be showing the microstructure of the iron oxides, although some amount of sulfur can be seen in location b. The S235 coupon sample from Figure 6.33 was cross-sectioned and examined further. Figure 6.34 shows the selected locations for chemical composition analysis and the analysis are listed in Table 6.24

Figure 6.34: Cross-sectioned SEM images of carbon steel S235 where the chemical composition analysis were performed, the areas indicated with red boxes.

Table 6.24: XEDS analysis of the cross-sectioned carbon steel S235 from Figure 6.34 [Weight%].

Location	O	S	Mn	Fe
a (bulk)			0.6	99.4
b (inner scale)	9.9	29.9	0.1	60.1
c (mid scale)	11.0	29.5	0.1	59.4
d (outer scale)	5.1	35.6	0.1	59.2

Table 6.24 shows that oxygen (O) and sulfur (S) were present in the corrosion product. The corrosion was believed to be iron sulfides and iron oxides. HIC damanges were present in the middle of the coupon. Figure 6.35 shows the HIC damages and the locations for chemical composition analysis. The analysis are listed in Table 6.25

(a)

(b)
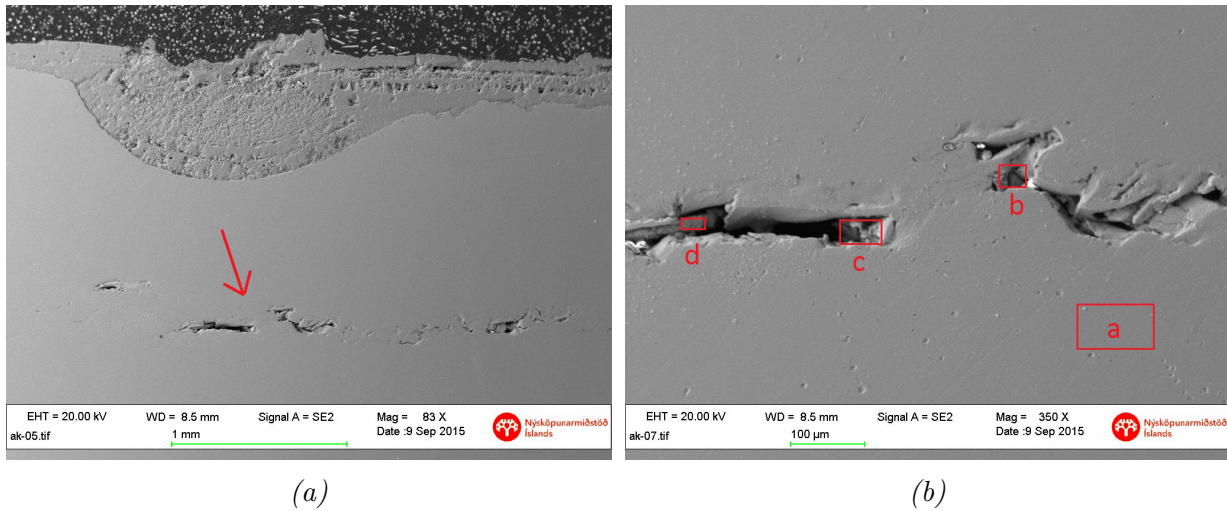
Figure 6.35: SEM images of the HIC damages after 12 weeks testing where the chemical composition analysis were performed, the areas indicated with a red box.

Table 6.25: XEDS analysis of the cross-sectioned carbon steel S235 from Figure 6.34 [Weight%].

Location	C	O	Si	Mn	Fe
a (bulk)			0.1	0.5	99.4
b (HIC hole)		8.7	18.1	0.8	72.4
c (HIC hole)	2.8	22.5	2.3	0.8	71.6
d (HIC hole)		1.9	0.3	0.7	97.1

Table 6.25 shows that there is some silica (Si) and carbon (C) present in the HIC hole, believed to be from polishing and the bakelite. High amounts of oxygen were found inside the holes and on the loose material around them. It is possible that water got into the holes when polishing and was not successfully cleaned out. The samples were inside the desiccator for three weeks waiting to be examined because of a failure in the SEM machine, it could be possible that during that time some iron oxides were able to form inside the holes. Also, it could be possible iron oxides, a corrosion product from oxygen ingress into the HIC crack during testing. The hydrogen diffusion into the BCC structure of the carbon steel and the pressure when two H react and form H_2 were the causes of these cracks/holes.

Figure 6.36 shows a microscopic view of the specimens after cleaning. The three coupons used for weight loss measurement were photographed and are shown below, all the samples had severe corrosion damages and two of the showed massive material loss. Holes in the material from HIC are visible in the thinned samples.

(a) S235   *(b) S235*   *(c) S235*
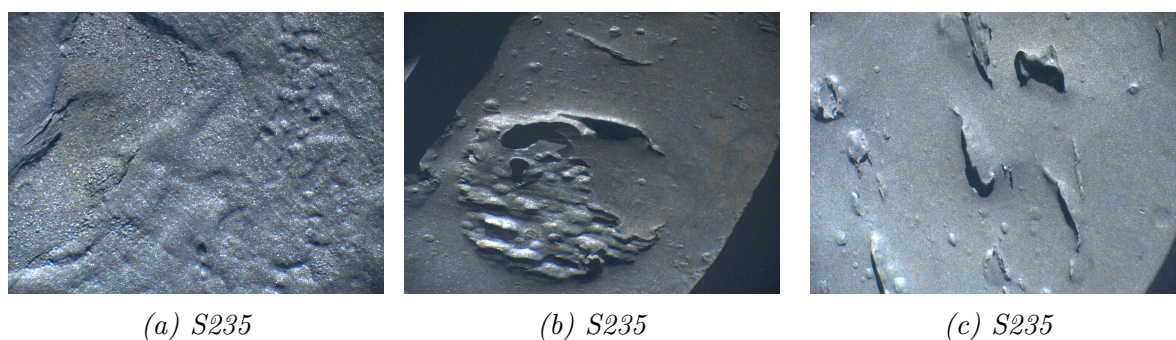
Figure 6.36: Microscopic images of carbon steel S235 surface after cleaning showing sever corrosion damages due to HIC.

316L coupon

316L sample was surface analysed before it was cross-sectioned . Figure 6.37 shows the surface of the specimen were the scaling is clearly noticed. The surface was not fully covered with the scale, as the bare metal could be identified. XEDS analysis were made on the surface to identify the chemical composition of the scaling on the 316L sample. Figure 6.37 and Table 6.26 show the chemical composition analysis and locations from the surface analysis. Figure 6.37 shows that the scaling is not covering the whole surface of the specimen.

(a)   *(b)*
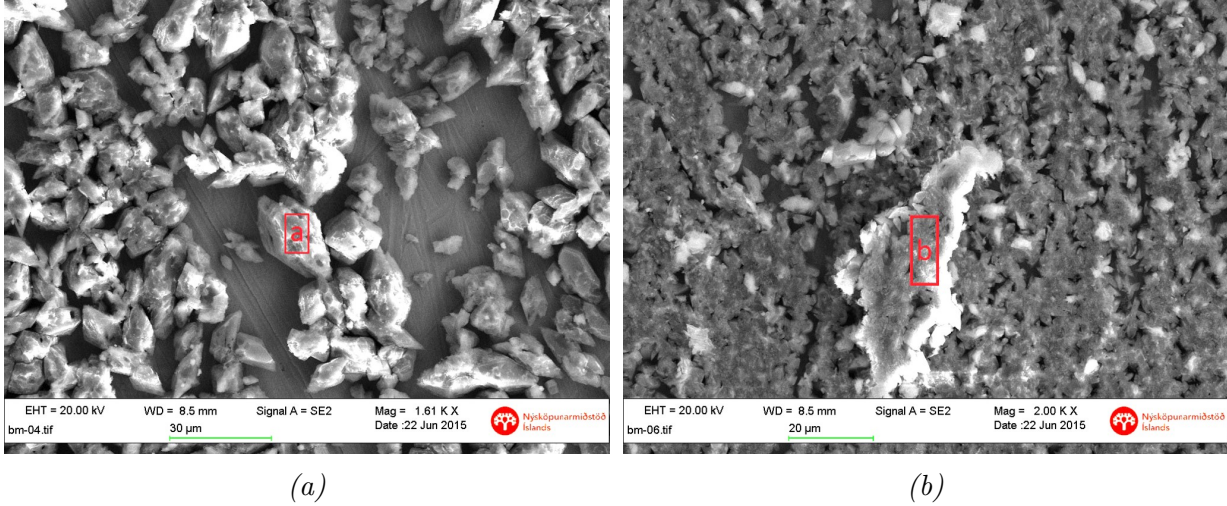
Figure 6.37: SEM images of the surface of austenitic stainless steel 316L after the 12 weeks testing where the chemical composition analysis were performed, the areas indicated with a red box.

Table 6.26: XEDS results of the surface of austenitic stainless steel 316L specimen from Figure 6.37 [Weight%].

Location	S	Fe
a	98.6	1.4
b	99.3	0.7

Table 6.26 shows that the scaling layer on the surface was mostly sulfur. Table 6.26 shows some amount of iron (Fe) in the scale that can be considered as corrosion products or iron sulfide (FeS) traces from the surrounding carbon samples. It was also possible that the XEDS was analysing the metal under the scaling layer because the layer was very thin. The 316L coupon was cross-sectioned and viewed in SEM. While cutting the specimen, care was taken that it would not heat to much. Cooling water could not be used as it was believed to clean the scaling layer of the sample. However, some sulfuric smell was detected coming from the sample and some heat generated in the sample. Figure 6.38 shows an overview of the samples surface as well as locations chosen for chemical composition analysis.
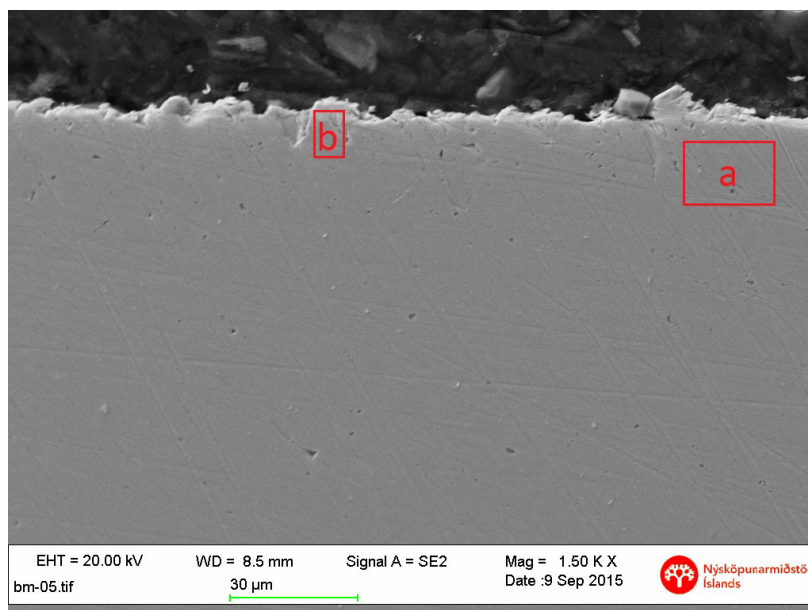
Figure 6.38: Cross-sectioned SEM image of the austenitic stainless steel 316L where the chemical composition analysis were performed, the areas indicated with a red box.

Table 6.27: XEDS analysis of the cross-section of the stainless steel 316L from Figure 6.12 [Weight%].

Location	O	Cr	Mn	Fe	Ni	Mo
a (bulk)		16.7	1.5	70.3	9.4	2.1
b (surface)	1.6	16.1	1.7	68.7	9.8	2.1

The chemical compositions shows that there might be some chromium oxide at the surface. No corrosion nor the scaling layer was found on the sample.

2205 coupon
The surface of duplex stainless steel 2205 was examined with SEM and XEDS. Figure 6.39 shows an overview of the surface scaling and the locations chosen for chemical composition analysis of the scale.

(a)   *(b)*
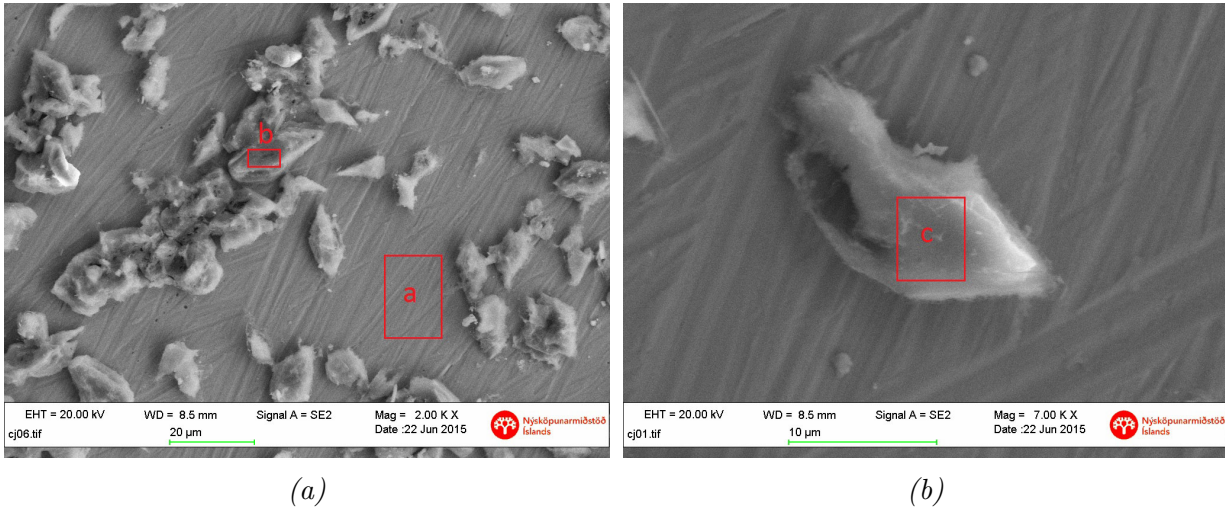
Figure 6.39: SEM images of the surface of duplex stainless steel 2205 after 12 weeks testing where the chemical composition analysis were performed, the areas indicated with a red box.

Table 6.28: XEDS results of the surface of duplex stainless steel 2205 specimen after 12 week testing from Figure 6.39 [Weight%].

Location	C	S	Si	Cr	Mn	Fe	Ni
a (bulk)		1.5	0.5	21.9	2.0	67.3	6.8
b (scale)	2.2	90.7		2.3		4.8	
c (scale)		83.6		4.4		11.0	1.0

Table 6.28 shows the chemical composition from the surface analysis. The analysis show the sulfur deposits on the surface and the chemical composition analysis show that chromium (Cr), iron (Fe) and nickel (Ni) deposits are in the scale. That might indicate some corrosion products in the scale or that the XEDS measures went through the scale and into the metal because of how thin the scale was.
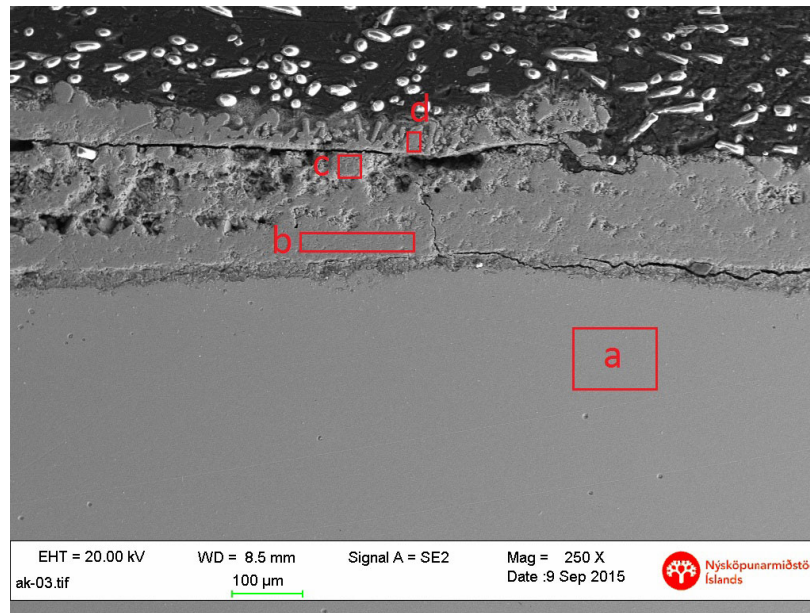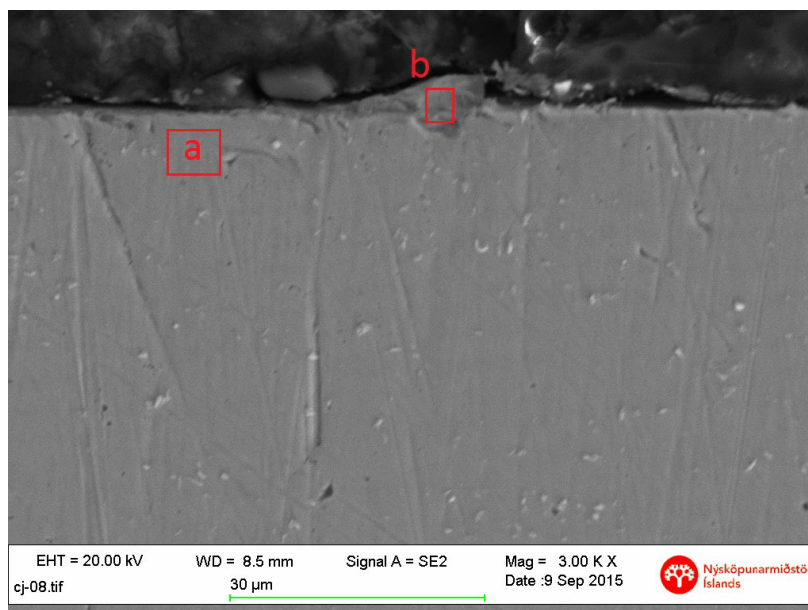
Figure 6.40: Cross-sectioned SEM image of duplex stainless steel 2005 where the chemical composition analysis were performed, the areas indicated with a red box.

Table 6.29: XEDS analysis of the cross-sectioned duplex stainless steel 2205 from Figure 6.14 [Weight%].

Location	O	Ca	Cr	Mn	Fe	Ni	Mo
a (bulk)			23.1	1.6	67.2	4.2	3.9
b (artefact)	3.6	1.4	25.6	2.8	63.5	2.6	0.5

Table 6.29 shows the chemical composition of the selected locations. No corrosion or pits could be found on the sample. However, the analysis from the artefact were believed to show that there were some chromium oxides present at the surface.

6.3.2. U-bend - Results

Similar as before the samples were cut so that there would be less heat generated as in previous 4 weeks tests. This was done so that the sulfur layer on the surface could be visible in cross-sectioned samples when viewed in SEM.

The austenitic stainless steel 304L continued to show cracks when examined with SEM. The cracks are much more severe, larger and distributed over a larger area compared to the 4 week cracks, the area can be seen in Figure 6.41. Figure 6.42 shows the selected location for chemical composition and the results are shown in Table 6.30.
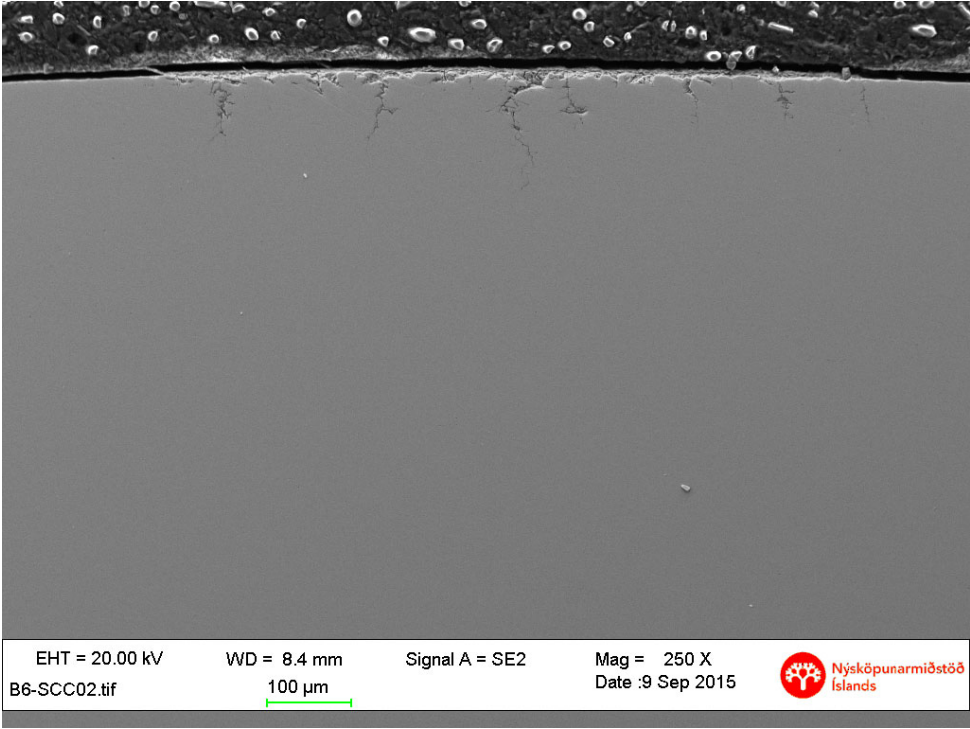
(a)
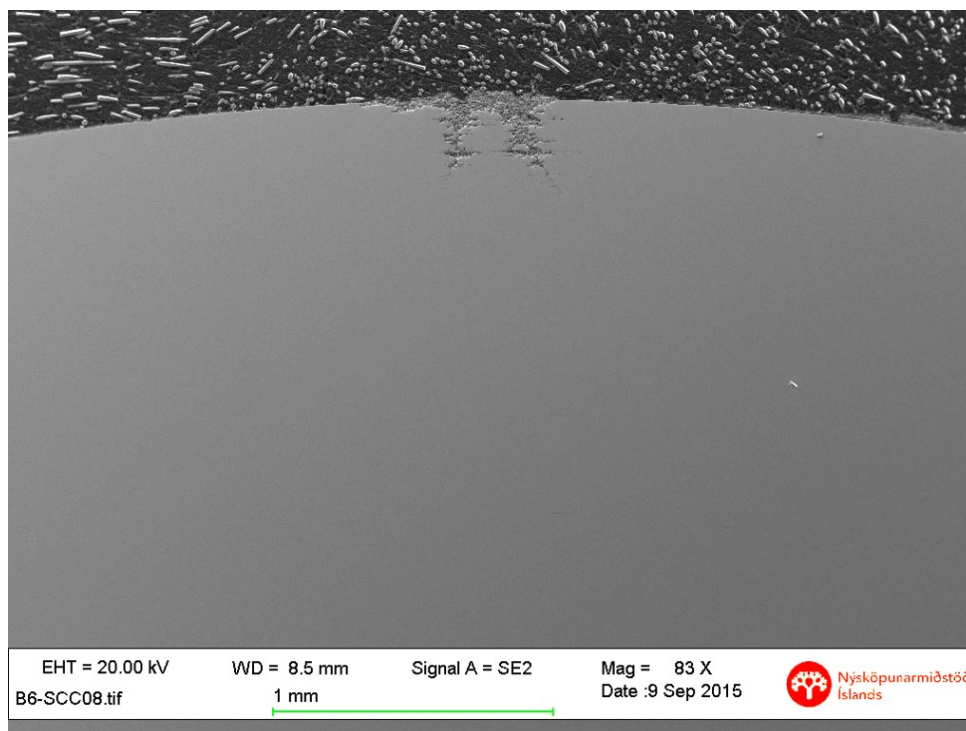
(b)

Figure 6.41: SEM images of the surface of austenitic stainless steel 304L showing the distribution of the cracks over the tension region of the sample.
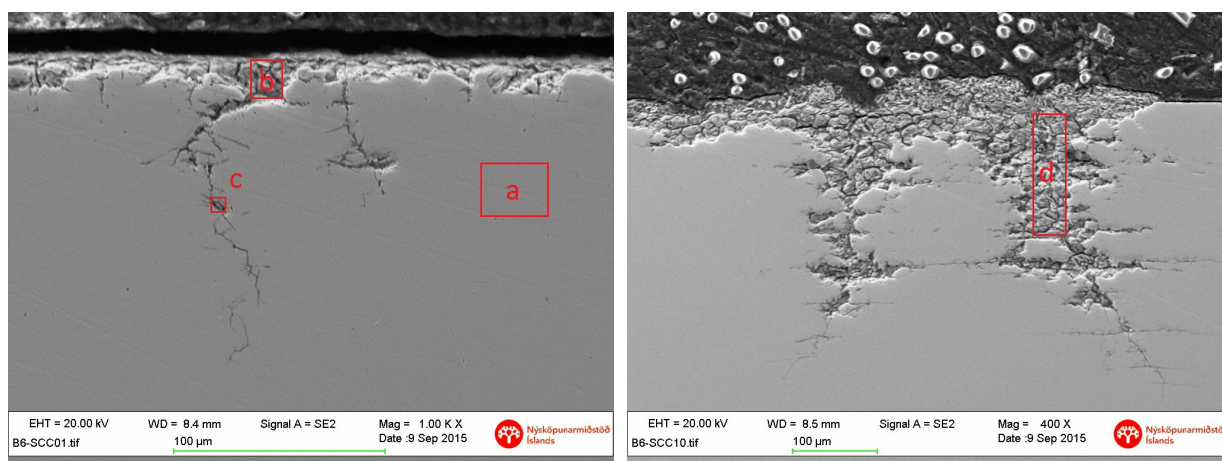
(a)   *(b)*

Figure 6.42: SEM images of the surface of austenitic stainless steel 304L sample after 12 weeks testing where the chemical composition analysis were performed in the cracks, the areas indicated with a red box.

Table 6.30: *XEDS analysis of the from Figure 6.42 [Weight%].*

Location	O	S	Cr	Mn	Fe	Ni	Mo	Cu
a (bulk)	1.2		17.7	1.9	71.3	7.5	0.4	
b (pit)	18.0	27.9	12.1	0.6	20.1	20.6		0.7
c (crack)	11.6	22.6	13.5	1.0	30.2	20.1		1.0
d (pit/crack)	21.0	44.0	4.1		2.3	27.4		1.2

High contents of sulfur (S), nickel (Ni) and oxygen (O) were seen in the corrosion products inside the crack. The analysis show that alloy underwent EIC cracking damages such as, SCC or SSC.

Chemical composition analysis for 316L U-bent specimens are shown in Figure 6.43 and Table 6.31

(a)   (b)
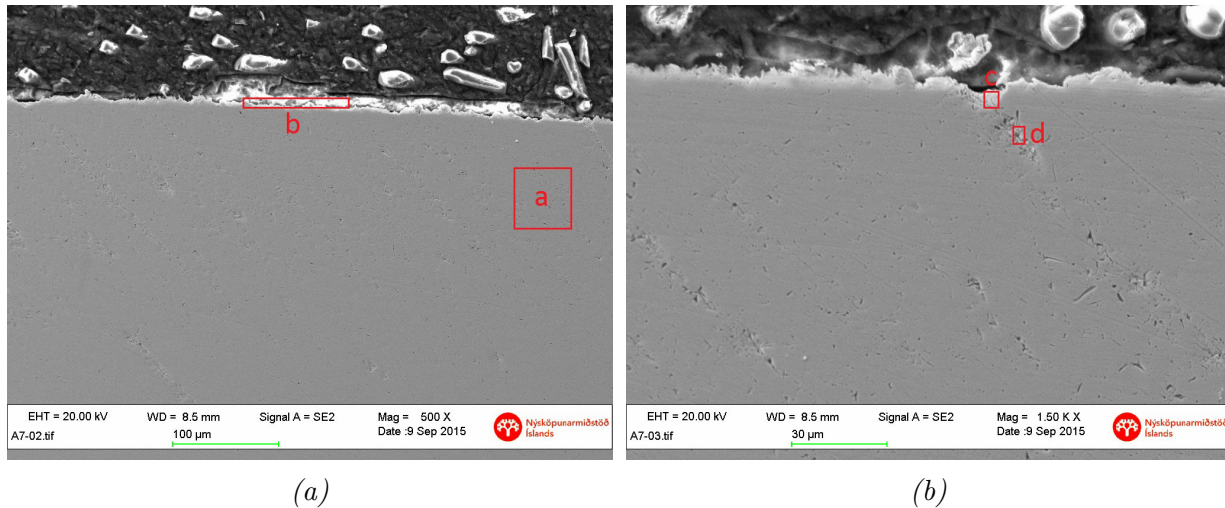
Figure 6.43: *SEM images of the surface of U-bent 316L specimens after 12 weeks testing where the chemical composition analysis were performed, the areas indicated with a red box.*

Table 6.31: *XEDS analysis of the cross-sectioned U-bent specimen 316L from Figure 6.43 [Weight%].*

Location	C	O	S	Cr	Mn	Fe	Ni	Mo
a (bulk)		1.6		16.4	1.6	68.8	9.4	2.2
b (scale)	8.3		90.5	0.2		1.0		
c (artefact)		4.1	2.6	15.4	1.6	66.8	9.5	
d (artefact)		3.6		16.3	1.5	67.3	9.1	2.2

The chemical composition analysis show that the scaling on the surface might have small amount of corrosion products since chrome (Cr) and iron (Fe) were identified. However, sulfur is dominant in the analysis and the carbon identified was considered to be from the bakelite. Several areas were found that could be interpreted as pit initiations but the analysis show that these are most possible artefacts. However, similar areas were found on the 304L specimen in the first test from section 6.1.2 where no cracks were identified after 4 weeks of testing, therefore, longer test time is required to verify the absence of cracks for 316L.

6.3.3. Summary

Carbon steel S235 showed iron oxides and iron sulfides corrosion products. Corrosion rate for the stainless steels 316L og 2205 showed very low corrosion rate if any. Severe crackings were found on the 304L sample. The cracks were distributed over the tensioned region and showed significantly more cracks than for the second 4 week test. Carbon steel S235 showed similar corrosion as in previous test. However, two sample were highly corroded compared to one in the previous tests. The highly corroded samples were on a different location compared to the previous tests on the specimen holder. The highly corroded samples had become very thin. Corrosion rate for the carbon steel was lower for the 12 week test. That is believed to be normal because the corrosion rate decreases since the corrosion products protect the bare metal at some rate. HIC damages were similar to those found in previous tests.

6.4. Additional carbon tests

Because of large difference in weight loss of carbon specimens with different locations on the specimen holder two additional tests were done to investigate this. The first test involved putting only S235 coupon samples on the specimen holder to see how the CR would change with location on the holder. The second test was done to investigate whether the effect of the existence of the stainless steel had any effect in increasing corrosion rate. two samples were located between 316L and two between duplex 2205. Figure 6.44 shows the installation of the coupons for these tests.
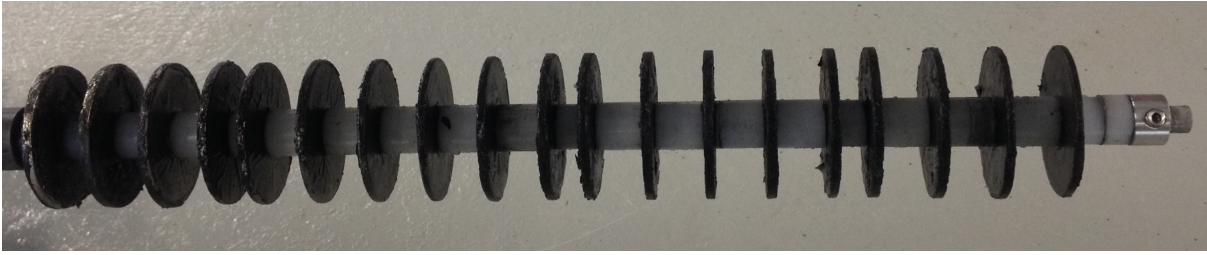
(a) Carbon test 1. All samples on the specimen holder are carbon steel S235.
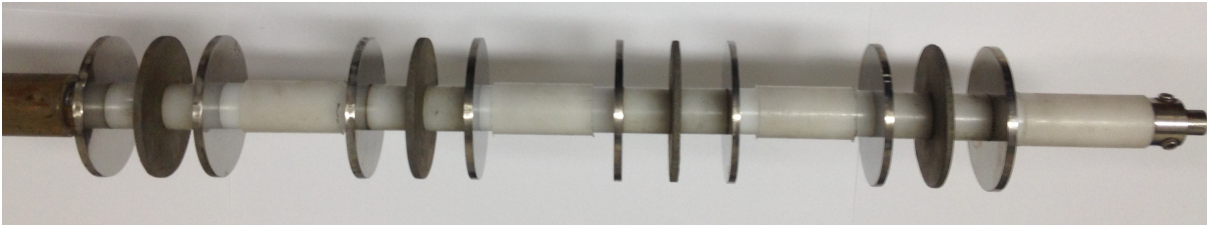
(b) Carbon test 2. S235 samples located between stainless steels, first two on the left placed in between 316L coupons and the first two on the right have S235 samples placed in between duplex 2205

Figure 6.44: S235 Coupon samples on the specimen holder for the additional tests.

6.4.1. Test 1

S235 samples were handled as mentioned in Section 5.2 about specimen handling. An overview of the air cleaning stations performance was collected and is shown in Table 6.32.It should be noted here that some difference existed in the operation of the air cleaning station between previous tests and test 1. When the samples were inserted into the station an stress testing was being performed for the air cleaning station, 60 l/s of condensed water was being pumped through the absorption tower for nearly 22 hours. Few days after the stress testing the station was being injected with non-condensible gases from an additional turbine (4 turbines in total) which was oxygen contaminated increasing the oxygen percentage of volume up to nearly 3%. Gas samples were taken and can be seen in Table A.1 in Appendix A. Gas samples for this experiment were taken June 8 (8.6.2015).

Table 6.32: Overview of Air cleaning station during first carbon steel experiment [hours].

Total	Running	Stop	System under stress testing	Gas coming from one added turbine
432.5	415.42	17.08	21.92	144

All the samples were weighed before installation and the samples that had the correct 15 mm spacing between each other were cleaned and weight after the test as in previous experiments. The S235 coupons showed signs of high corrosion rate but one sample being more corroded than the other remaining samples was not as eye catching as in previous tests. However two samples near the absorption tower wall showed lower corrosion rate at about 2.7 and 3.1 mm/yr while the other remaining samples showed corrosion rates of 4-7 mm/yr. HIC damages were visible on all of the samples. Corrosion rate for all the samples is shown in Table B.2 in Appendix B. Average corrosion rate for this experiment was ≈4.96 mm/yr. Figure 6.45 shows the corrosion rate vs location inside the absorption tower for this experiment. It is clear that near the wall the corrosion rate is lower.
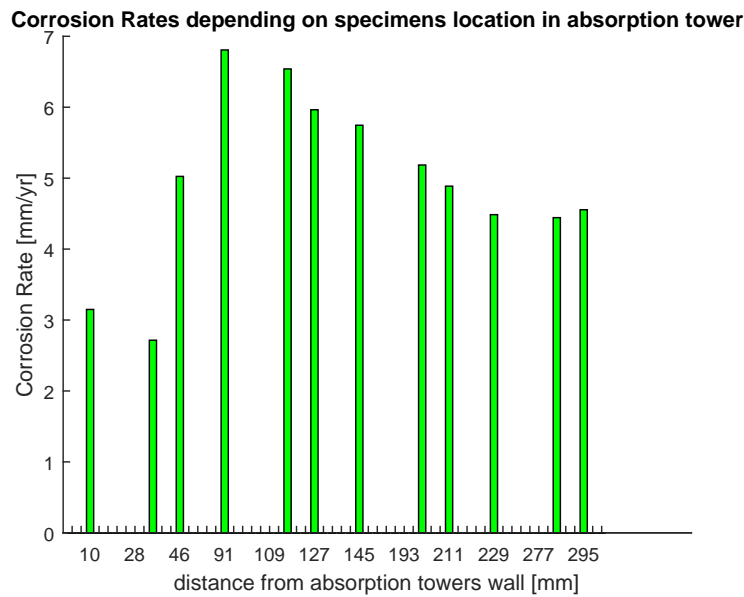
Figure 6.45: Corrosion rates for carbon test 1 vs location inside the absorption tower.

6.4.2. Test 2

After the results from the first carbon test four of the tested coupon samples were rinsed with acetone after the weight loss measurement, measured and inserted back into the absorption tower. The S235 coupon samples tested were located between stainless steel coupons, Figure 6.44b. The samples were inserted while the station was running, few stops occurred during this test.

Table 6.33: Overview of Air cleaning station during first carbon steel experiment [hours].

Total	Running	Stop
408	351.5	56.5

Carbon steel samples were weight loss measured after testing showing an average corrosion rate up to 2.70 mm/yr. Corrosion rate calculations for the tested samples in this test 2 can be seen in Table 6.33. The corrosion rate for this experiment is compared to carbon test 1 in Figure 6.46.
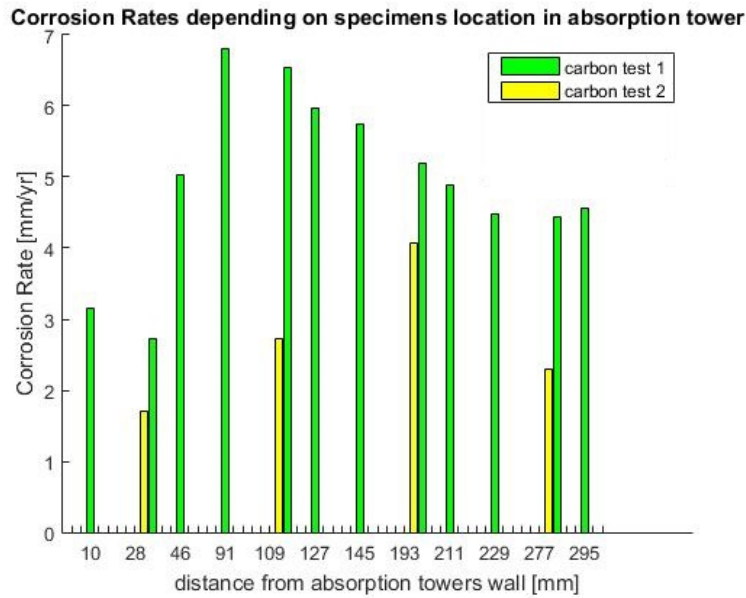
Figure 6.46: Comparison on corrosion rates for carbon test 1 and 2.

7. Discussion

The air cleaning system had several stoppages during this experiment. It is well known that stagnant conditions can lead to pitting or SCC (Karlsdóttir, 2012). When the system shuts down no gas or water goes in and out of the tower. However, some sour water will be stationary at the bottom of the tower. Thus, the stagnant conditions formed in these stoppages can be considered a threat. The environment inside the absorption tower is unusual compared to normal geothermal conditions. The difference is mostly due to the high amount of H_2S in the tower which can increase the corrosion effect.

The stainless steel 316L showed no sign of corrosion rate or corrosion failure for both the coupon and the U-bend tests. According to the lead designer of the air cleaning station, Magnús Þór Arnarson, austenitic stainless steel 304L is preferably not used in design where it gets in contact with gases or liquid with dissolved gases. At the site, pipes made of 316L have been showing leakages, believed to be from bad welding, where the sour liquid was able to sit at low points. Heat exchanger made from 316 Ti also failed, believed to be in from bad welding or near the welding area (Arnarson, 2015). The 304L stainless steel showed severe cracking formations, especially for the 12 week test. It was believed that the high amount of H_2S in the tower played a major role in cracking formation. The cracking was believed to be a form of EIC because the samples were specially designed for SCC testing but it is hard to rule out SSC. In fact, the cracking might be a combination of both (Kane & Cayard, 1998). 316L U-bend samples showed no signs of corrosion damages and the new absorption tower was constructed correctly to avoid welding defects capable of creating stagnant conditions that can lead to failure. Prakash et al. (1999) found 316L to be immune to SCC under similar conditions containing 5% NaCl. However, the experience from the 304L first test which did not show any SCC, but possible initiations shows that longer testing time might be required for 316L. Several locations in 316L samples showed artefacts from cross-sectioning and mounting of the samples that could be misinterpreted for pit initiations but the chemical composition analysis and the microstructural analysis of the surface did not indicate any pitting formation which supports that.

The scaling that forms on the surface of the stainless steels can be considered to be mostly sulfur according to XEDS analysis. Smith & Craig (2005) reported that for gas phase the reaction of H_2S in an oxygen contaminated environment could occur. Where the reaction would be:

$$H_2S + O_2 \rightarrow S + H_2O \tag{7.1}$$

This is believed to be the scaling formed on the surface of the stainless steels. The chemical composition analysis from this experiment showed traces of chromium (Cr) and iron (Fe)

in the sulfur scaling. The chromium (Cr) and iron (Fe) contents in the analysis could be corrosion products in a very small scale or a corrosion products from the surrounding samples. The corrosion rate analysis showed that 316L and 2205 were performing very well under these conditions.

Carbon steel S235 shows significant ammount of corrosion and has an poor performance at the absorption tower. It is commonly known that H_2S and/or CO_2 containing environments can be very aggressive to carbon and low alloyed steels and wet H_2S environment has been associated with internal blistering, hydrogen induced cracking and stress oriented hydrogen induced cracking(SOHIC) with carbon steels (Kane & Cayard, 1998). The corrosion damages found on the S235 samples are considered to be uniform and HIC corrosion. The corrosion layer is iron sulfides or iron oxides of the type Fe_xS_y, Fe_xO_y or $Fe_xS_yO_z$. Bai et al. (2014) reports that the established overall reaction between carbon steel and H_2S could be described as:

$$Fe + H_2S_{aq} \rightarrow FeS + H_2 \tag{7.2}$$

Moreover, Kane & Cayard (1998) reviews the behaviour of H_2S on engineering alloys, including carbon steels and reports that the molecular forms of these iron sulfide corrosion products can be either FeS_2, Fe_7S_8 or Fe_9S_8.

HIC damages similar to those in this experiment have been reported. Kittel et al. (2010) tested low-alloyed steels for HIC damages in sour environments where initiation of cracks were initiated at the center line of the specimens thickness similar to the HIC damages found in this experiment. Kittel et al. (2010) reports that the initiation of HIC depends significantly on the pH level and the partial pressure of the H_2S, However, Kittel et al. (2010) shows that the influence of both these aspects is not monotone. For example a higher H_2S partial pressure decreases the effects of HIC to the metal that could be explained by the build up of protective iron sulfide layer. Susceptibility of carbon steels to HIC has been reported at room temperature in a sour NACE solution saturated with H_2S. With increased temperature both the corrosion rate and the effects of HIC to the metal were decreased, believed to be caused by a reduction of H_2S concentration in the solution (Al-Anezi, 1999). It has also been reported that HIC occurs as the initial crack for SOHIC (Kim et al., 2010). Oxygen (O) was found present in the HIC damages. Possible iron oxides could be found in the damages, a corrosion product from oxygen ingress into the HIC crack during testing.

The acceptable corrosion rate limit is defined as 0.1 mm/yr (Lichti et al., 2010). The corrosion rates results for carbon steel are listed in Table 7.1.

Table 7.1: Corrosion Rate results for carbon steel.

Material Type	Corrosion Rate [mm/yr]	Average Corrosion Rate [mm/yr]
4 weeks Experiment 1	2.46 7.72 2.57	4.25
4 weeks Experiment 2	2.21 7.59 2.58	4.13
12 weeks Experiment	0.95 4.61 3.40	2.99

Table 7.2 describes the materials performance according to its corrosion rate. From the Table and the definition on acceptable corrosion rate our results show that the stainless steel show an outstanding performance with nearly no corrosion rate measured. The carbon steel shows poor performance according to Table 7.2. The corrosion rate for the first two 4 week experiments is very similar ($\approx$ 4.2 mm/yr) while for the 12 week experiment it is slightly less ($\approx$ 3 mm/yr). This is quite normal because the corrosion products form a layer on the surface that starts to protect the sample and lowers the corrosion rate.

Table 7.2: Relative corrosion resistance performance.

Relative Corrosion Resistance	mm/yr
Outstanding	< 0.02
Excellent	$0.02 - 0.1$
Good	$0.1 - 0.5$
Fair	$0.5 - 1$
Poor	$1 - 5$
Unacceptable	$5+$

Source: (Jones, 1996)

The influence of oxygen on carbon steel in the system can be clearly seen in the additional carbon tests. The corrosion rate is considerably higher for the test where gas was taken from the the additional oxygen contaminated turbine. Smith & Craig (2005) report that

oxygen can change the solutions chemistry and has a significant effects on the corrosion rate. It is also reported that the corrosion rates for H_2S environments (no O_2 or CO_2) are generally low, 0.5 mm/yr or less because of the protective iron sulfide film formed on the surface. Smith & Craig (2005) also report that the addition of CO_2 can significantly effect the corrosion rate since the corrosion rate is dominated by CO_2 and that the oxygen in the system can induce localized attack in the form of pitting and HIC.

The influence on the highly corroded samples found in the first three experiments is still unknown. When samples are inside the absorption tower there are hole plates above and below. These hole plates are believed to affect the distribution of the condensed water in the tower, causing one sample to be directly under a hole e.g. larger water drops fall on it. Another factor to consider from the additional carbon tests is that the corrosion rate is lower for the samples near the wall. This could also be described with the hole plates if the hole pattern does not go all the way to the wall, or it could be described with fluid mechanics, where friction from the walls lets the area near the walls be under less flow rate of condensed water, thus, lower impact and affects from the environment inside the tower. Figure B.1 in Appendix B shows the Corrosion rate vs location inside the absorption tower for all experiments where each bar represents a sample. It should be noted that the samples were not placed on the exact location between experiments, their position can vary for a few millimetres.

8. Conclusions

The absorption tower at Hellisheiði Power Plant is operating with condensed geothermal water ($\approx$35 kg/s) and non-condensible gases ($0.4 - 0.5$ kg/s) from the turbines at 5 bars and 20-25°C. The results from all these tests indicate that current material selection of austenitic stainless steel 316L for the absorption tower at Hellisheiði power plant is sufficient. The stainless steels 316L and 2205 showed no signs of corrosion damages for the corrosion rate experiment and the corrosion rate was hardly measured. 316L also indicated a resistance to SCC in the U-bent experiment. Pit initiations on the 304L sample from the first 4 week test could not be verified. However, stainless steel 304L experienced SCC cracking for the second 4 week test as well as the 12 weeks test, where the SCC cracking was distributed over a large area. The carbon steel showed high corrosion rate and underwent extensive HIC damages from hydrogen diffusion. The oxygen in the system along with CO_2 was believed to have significant effects on the high corrosion rate of the carbon steel as was evident in the additional testing on the carbon steels. In comparison to stainless steel 316L, carbon steel S235 and the austenitic stainless steel 304L were lacking in performance. Duplex stainless steel 2205 along with 316L indicated immunity to the environment.

For future work, longer exposure time for testing is needed to have more information on what to expect for the performance in the long run and what effects the sulfur (S) deposits might have on the 316L. Other types of experiments could be done, for example testing on welded samples to investigate accurately the resistance of the welds in the tower and pipes (which have been failing at the welded areas). Also it would be interesting to see if there is a difference in corrosion rate or SCC when the air cleaning system is stopped versus when it is up and running, to investigate the difference between stagnant conditions and flow conditions. Furthermore, Comparison between this project and corrosion experiments at the bottom of the absorption tower might be interesting. The concentration of H_2S and CO_2 is much higher at the bottom than in the middle. However, the oxygen concentration might be lower at the bottom.

References

Aalco. (2015a). *Stainless Steels (Stainless 304 Properties, Fabrication and Applications, Supplier Data by Aalco).* Retrieved 2015-08-09, from `http://www.azom.com/article.aspx?ArticleID=2867#_304L_Stainless_Steel`

Aalco. (2015b). *Stainless Steels (Stainless 316 Properties, Fabrication and Applications, Supplier Data by Aalco).* Retrieved 2015-08-09, from `http://www.azom.com/article.aspx?ArticleID=2868#_316L_Stainless_Steel`

Al-Anezi, M. (1999). Susceptibility of conventional pressure vessel steel to HIC and SOHIC in H2S diglycolamine solutions. *Corrosion*, *55*(11), 1101–1109.

Aradóttir, E. S., Gunnarsson, I., Sigfússon, B., Gunnarsson, G., Gunnlaugsson, E., Sigurðardóttir, H., . . . Sonnenthal, E. (2012). Towards cleaner geothermal energy utilization: Capturing and sequestering CO˜2 and H˜2S emissions from geothermal power plants. In *Though symposium.* Berkeley, California: Lawrance Berkeley National Laboratory.

Aradóttir, E. S. P., Gunnarsson, I., Sigfússon, B., Gíslason, S. R., Oelkers, E. H., Stute, M., . . . Gunnlaugsson, E. (2015). Towards Cleaner Geothermal Energy : Subsurface Sequestration of Sour Gas Emissions from Geothermal Power Plants. In *World geothermal congress.* Melbourne, Australia.

Arnarson, M. T. (2015, 18 August). [Personal Communication].

Bai, P., Zheng, S., Zhao, H., Ding, Y., Wu, J., & Chen, C. (2014). Investigations of the diverse corrosion products on steel in a hydrogen sulphide environment. *Corrosion Science*, *87*, 397–406. doi: 10.1016/j.corsci.2014.06.048

Banaś, J., Lelek-Borkowska, U., Mazurkiewicz, B., & Solarski, W. (2007, May). Effect of CO2 and H2S on the composition and stability of passive film on iron alloys in geothermal water. *Electrochimica Acta*, *52*(18), 5704–5714. doi: 10.1016/j.electacta.2007.01.086

Bertani, R. (2012). Geothermal power generation in the world 2005-2010 update report. *Geothermics*, *41*(2012), 1–29. doi: 10.1016/j.geothermics.2011.10.001

Bertani, R. (2015). Geothermal Power Generation in the World 2010–2014 Update Report. In *World geothermal congress.* Melbourne, Australia.

REFERENCES

Chaves, R. B. (1996). *Geothermal gases as a source of commercial CO2, in Miravalles, Costa Rica and Haedarendi, Iceland* (Tech. Rep.). Reykjavík, Iceland: The United Nations University.

Conover, M., Ellis, P., & Curzon, A. (1980). Material Selection Guidelines for Geothermal Power Systems - An Overview. In L. Casper & T. Pinchback (Eds.), *Geothermal scaling and corrosion* (pp. 24–40). American society for testing and materials.

Corsi, R. (1986). Scaling and corrosion in geothermal equipment: problems and preventive measures. *Geothermics*, *15*(5-6), 839–856. doi: 10.1016/0375-6505(86)90097-0

Davoodi, a., Pakshir, M., Babaiee, M., & Ebrahimi, G. (2011). A comparative H2S corrosion study of 304L and 316L stainless steels in acidic media. *Corrosion Science*, *53*(1), 399–408. doi: 10.1016/j.corsci.2010.09.050

Ding, J., Zhang, L., Li, D., Lu, M., Xue, J., & Zhong, W. (2013). Corrosion and stress corrosion cracking behavoir of 316L austenitic stainless steel in high H2S-CO2-CL- environment. *Journal of Materials Science*, *48*(10), 3708–3715. doi: 10.1007/s10853-013-7168-1

Farison, J., Benn, B., & Berndt, B. (2010). Geysers Power Plant H2S Abatement Update. *GRC Transactions*, *34*.

G1-90, A. (1999). *Standard practice for preparing, cleaning, and evaluating corrosion test specimens* [Standard]. ASTM International. Retrieved from `www.astm.org` doi: 10.1520/G0001-90R99E01

G30-97, A. (2009). *Standard practice for making and using u-bend stress-corrosion test specimens* [Standard]. ASTM International. Retrieved from `www.astm.org` doi: 10.1520/G0030-97R09

G4-01, A. (2001). *Standard guide for conducting corrosion test in field applications* [Standard]. ASTM International. Retrieved from `www.astm.org` doi: 10.1520/G0004-01

G46-94, A. (2013). *Standard guide for examination and evaluation of pitting corrosion* [Standard]. ASTM International. Retrieved from `www.astm.org` doi: 10.1520/G0046

Gilbert, N. (2014). *Structural Steel (S235, S275, S355 Chemical Composition, Mechanical Properties and Common Application).* Retrieved 2015-08-08, from `http://www.azom.com/article.aspx?ArticleID=6022`

Goldstein, J. I., Newbury, D. E., Echlin, P., Joy, D. C., Lyman, C. E., Lifshin, E., . . . Michael, J. R. (2003). *Scanning Electron Microscopy and X-ray Microanalysis* (3rd ed.). Springer.

Gunnarsson, I. (2015, 20 August). [Personal Communication].

Gunnarsson, I., & Aradóttir, E. (2013). Geothermal Gas Emission From Hellisheiði and Nesjavellir Power Plants, Iceland. *GRC Transactions*, *37*.

Gunnarsson, I., Júlíusson, B. M., Aradóttir, E. S., Sigfússon, B., & Arnarson, M. T. (2015). Pilot Scale Geothermal Gas Separation, Hellisheiði Power Plant Iceland. In *World geothermal congress.* Melbourne, Australia: Reykjavík Energy.

He, W., Knudsen, O., & Diplas, S. (2009). Corrosion of stainless steel 316L in simulated formation water environment with CO2-H2S-Cl-. *Corrosion Science*, *51*(12), 2811–2819. doi: 10.1016/j.corsci.2009.08.010

Javaherdashti, R., Nwaoha, C., & Tan, H. (2013). *Corrosion and Materials.* Taylor & Francis Group.

Jones, D. A. (1996). *Principles and prevention of corrosion* (2nd ed.). Upper Saddle River, NJ 07458: Prentice-Hall Inc.

Kane, R., & Cayard, M. (1998). Roles of H2S in the Behavior of Engineering Alloys: A Review of Literature and Experience. *CORROSION*(274), 28.

Karlsdóttir, S. N. (2012). Corrosion, scaling and material selection in geothermal power production. In *Comprehensive renewable energy* (1st ed., Vol. 7, pp. 241–259). Elsevier Ltd. doi: 10.1016/B978-0-08-087872-0.00706-X

Kaya, T., & HoShan, P. (2005). Corrosion and material selection in geothermal systems. In *World geothermal congress.* Antalya, Turkey.

Kim, W. K., Jung, H. G., Park, G. T., Koh, S. U., & Kim, K. Y. (2010). Relationship between hydrogen-induced cracking and type I sulfide stress cracking of high-strength linepipe steel. *Scripta Materialia*, *62*(4), 195–198. doi: 10.1016/j.scriptamat.2009.10.028

Kittel, J., Smanio, V., Fregonese, M., Garnier, L., & Lefebvre, X. (2010). Hydrogen induced cracking (HIC) testing of low alloy steel in sour environment: Impact of time of exposure on the extent of damage. *Corrosion Science*, *52*(4), 1386–1392. doi: 10.1016/j.corsci.2009.11.044

Landolt, D. (2007). *Corrosion and Surface Chemistry of Metals.* EPFL Press.

Lichti, K. A. (2007). *Forgotten phenomenon of materials selection and use in geothermal energy applications* (Vol. 24) (No. 4). doi: 10.3184/096034007X282702

Lichti, K. A., White, S. P., Ko, M., Villa, R. R., Siega, F. L., Olivar, M. M. M., . . . Onega, M. S. (2010). Acid Well Utilisation Study : Well MG-9D , Philippines. In *World geothermal congress.* Bali, Indonesia.

Lu, Z., Gao, Z., & Fang, D. (2005). Stress Corrosion Susceptibility of 316L Stainles Steel in H2S and Cl Aqueous Solution. *Journal of Pressure Equipment and Systems*, *3*, 45–48.

Matek, B. (2014). *2014 Annual U.S. & Global Geothermal Power Production Report* (Tech. Rep.). Geothermal Energy Association.

REFERENCES

Materials, A. (2014). *Stainless Steel (Grade 2205 Duplex (UNS S32205)).* Retrieved 2015-08-09, from `http://www.azom.com/article.aspx?ArticleID=958`

Nagl, G. J. (2009). Coso Geothermal Field - 15 Years of Successful H2S Emission Abatement. *GRC Bulletin*(December), 21–24.

Nagl, G. J. (2010). H 2 S Emission Controlling emissions keeps a geothermal power facility. *Pollution engineering*(May), 38–42.

Olafsdottir, S., & Gardarsson, S. M. (2013). Impacts of meteorological factors on hydrogen sulfide concentration downwind of geothermal power plants. *Atmospheric Environment*, *77*, 185–192. doi: 10.1016/j.atmosenv.2013.04.077

Orkuspárnefnd. (2014). *Raforkuspá 2014-2050: Endurreikningur á spá frá 2010 út frá nyjum gögnum og breyttum forsendum* (Tech. Rep.). Reykjavik: Orkustofnun.

Papic, P. (1991). *Scaling and corrosion potential of selected geothermal waters in Serbia* (Tech. Rep.). Reykjavík, Iceland: The United Nations University.

Popoola, L., Grema, A., Latinwo, G., Gutti, B., & Balogun, A. (2013). Corrosion problems during oil and gas production and its mitigation. *International Journal of Industrial Chemistry*, *4*(1), 35. doi: 10.1186/2228-5547-4-35

Prakash, T. L., Hara, J. O., & Malik, A. U. (1999). (SCC) Behavior of Various Metals and Alloys Used in the Desalination and Power Plants. *Environment*(October 1999), 13–18.

Ragnarsdóttir, K. R. (2013). *Corrosion Experiments In Dry Superheated Steam From IDDP-1* (MSc.). University of Iceland.

Ragnarsson, A. (2010). Geothermal Development in Iceland 2005-2009. In *World geothermal congress.* Bali, Indonesia.

Roberge, P. R. (2008). *Corrosion Engineering: Principles and Practice.* McGraw Hill. doi: 10.1036/0071482431

Roberge, P. R. (2012). *Handbook of corrosion engineering* (2nd ed.). McGraw Hill.

Sandvik. (2015a). *SANDVIK SAF 2205 (Tube and pipe, seamless).* Retrieved 2015-08-09, from `http://smt.sandvik.com/en/materials-center/material-datasheets/tube-and-pipe-seamless/sandvik-saf-2205/`

Sandvik. (2015b). *SANMAC 304/304L (Hollow bar).* Retrieved 2015-08-09, from `http://smt.sandvik.com/en/materials-center/material-datasheets/bar-and-hollow-bar/hollow-bar/sanmac-3043041/`

Sandvik. (2015c). *SANMAC 316/316L (Hollow bar).* Retrieved 2015-08-09, from `http://smt.sandvik.com/en/materials-center/material-datasheets/bar-and-hollow-bar/hollow-bar/sanmac-3163161/`

Sanopoulos, D., & Karabelas, A. (1997). Abatement in Geothermal Plants: Evaluation of Process Alternatives. *Energy Sources*, *19*(1), 63–77. doi: 10.1080/00908319708908833

Schweitzer, P. A. (2010). *Fundementals of corrosion mechanism,causes, and preventative methods.* Boca Raton, FL 33487-2742: Taylor & Francis Group.

Smith, L., & Craig, B. B. (2005). Practical Corrosion Control Measures for Elemental Sulfur Containing Environments. *CORROSION*(05646), 20.

Sprowls, D. O. (1987). Evaluation of Pitting Corrosion. In A. International (Ed.), *Asm handbook - corrosion* (Vol. 13, pp. 500–507). ASM International.

Stephens, F. B., Hill, J. H., & Phelps, P. L. (1980). *State-Of-The-Art Hydrogen Sulfide Control for Geothermal Energy Systems* (Tech. Rep.). U.S. Department of Energy. Retrieved from `http://igor.beg.utexas.edu/readingroom/fulltext.aspx?ID=53913`

Takahashi, K., & Kuragaki, M. (2000). Yanaizu-Nishiyama Geothermal Power Station H 2 S Abatement System. In *World geothermal congress* (pp. 719–724). Kyushu- Tohoko, Japan.

Thorolfsson, G. (2005). Maintenance History of a Geothermal Plant : Svartsengi Iceland. In *World geothermal congress.* Antalya, Turkey.

Thorsteinsson, T., Hackenbruch, J., Sveinbjörnsson, E., & Jóhannsson, T. (2013). Statistical assessment and modeling of the effects of weather conditions on H2S plume dispersal from Icelandic geothermal power plants. *Geothermics*, *45*, 31–40. doi: 10.1016/j.geothermics.2012.10.003

Verkefnisáætlun SulFix: Um förgun brennisteinsvetnis frá jarðgufuvirkjunum. (2013). In *a meeting held by orkuveita reykjavíkur 20. february.* Orkuveita Reykjavíkur (Reykjavík Energy).

World Energy Council. (2013). *World Energy Resources.* London: World Energy Council.

World Environment Center. (1994). *Technical Assessment on H2S Gas Abatement Systems At California Energy 's Coso Geothermal Power Plants* (Tech. Rep.). Philippines: US - ASIA Environmental Partnership.

A. Chemical Analysis on Gas and Condensed Water

Table A.1: Chemical analysis of gases going to the air cleaning station (% of volume).

Date	Sample nr	H_2	O_2	N_2	CH_4	CO_2	H_2S
28.6.2014	14-5204	16.2	0.1	1.5	0.4	61.5	24.5
11.7.2014	14-5219	15.6	2.1	9.0	0.4	57.6	21.2
21.7.2014	14-5242	17.6	0.2	1.6	0.4	59.7	27.2
11.8.2014	14-5263	15.3	1.0	5.6	0.5	60.9	19.0
18.8.2014	14-5283	15.1	0.9	4.1	0.4	60.4	20.9
21.8.2014	14-5290	18.4	1.5	8.9	0.5	58.3	19.9
15.9.2014	14-5294	16.0	1.8	7.6	0.4	52.7	23.6
15.9.2014	14-5298	17.0	1.7	7.1	0.4	54.5	20.9
23.9.2014	14-5329	16.6	0.3	2.1	0.4	59.0	24.0
30.9.2014	14-5343	15.0	1.5	6.5	0.4	56.6	25.5
2.10.2014	14-5347	16.7	1.6	7.5	0.4	55.5	24.8
19.1.2015	15-5035	17.1	1.2	5.7	0.4	56.1	26.6
15.4.2015	15-5246	19.1	0.7	3.6	0.6	54.8	27.8
6.5.2015	15-5257	17.4	5.4	22.0	0.5	46.7	19.9
13.5.2015	15-5267	19.4	0.4	2.4	0.5	59.0	27.5
1.6.2015	15-5279	15.3	0.4	2.5	0.4	56.1	26.0
1.6.2015	15-5281	14.8	0.4	2.4	0.4	55.4	28.4
1.6.2015	15-5284	15.4	0.5	2.9	0.5	56.7	24.3
1.6.2015	15-5287	16.0	0.5	3.0	0.5	56.1	28.0
2.6.2015	15-5290	15.7	0.6	3.2	0.5	55.3	25.1
3.6.2015	15-5305	15.5	0.5	3.1	0.5	55.3	26.9
3.6.2015	15-5318	17.4	0.5	3.1	0.5	54.9	27.2
8.6.2015	15-5321	14.9	2.9	12.4	0.4	48.8	22.7

Table A.2: Chemical analysis of gases going from the air cleaning station (% of volume).

Date	Sample nr	H_2	O_2	N_2	CH_4	CO_2	H_2S
28.6.2014	14-5203	36.3	0.3	3.4	0.8	57.9	1.7
11.7.2014	14-5220	30.0	3.1	14.2	0.7	53.7	1.3
18.8.2014	14-5284	40.9	2.1	10.8	1.1	45.7	0.5
2.10.2014	14-5348	33.9	2.7	12.7	0.7	50.7	1.2
19.1.2015	15-5036	29.0	2.3	10.2	0.6	55.5	4.0
15.4.2015	15-5245	37.0	1.2	6.6	0.9	53.7	2.1
13.5.2015	15-5266	39.1	0.1	4.6	1.0	58.3	1.4
1.6.2105	15-5280	32.0	0.9	5.2	0.9	51.1	1.1
1.6.2105	15-5282	35.3	0.9	5.7	0.9	48.2	1.0
1.6.2105	15-5285	42.0	1.2	7.7	1.3	43.8	0.7
1.6.2105	15-5288	45.6	1.2	8.1	1.3	37.9	0.4
2.6.2105	15-5291	48.4	1.4	8.9	1.3	30.4	0.4
2.6.2105	15-5293	55.2	1.6	10.3	1.5	23.5	0.2
2.6.2105	15-5295	30.8	0.9	5.5	0.8	55.3	3.8
2.6.2105	15-5297	26.0	0.7	4.9	0.8	58.1	5.3
2.6.2105	15-5299	24.9	0.8	4.8	0.7	58.5	7.6
2.6.2105	15-5301	22.6	0.7	4.2	0.7	58.8	11.9
2.6.2105	15-5303	20.4	0.7	4.2	0.6	57.6	18.4
3.6.2015	15-5306	35.5	1.2	7.0	1.0	48.7	2.0
3.6.2015	15-5308	42.5	1.4	8.4	1.3	45.3	1.5
3.6.2015	15-5310	22.6	0.8	5.1	0.7	58.8	10.8
3.6.2015	15-5312	26.1	1.0	5.9	0.9	58.7	8.5
3.6.2015	15-5314	26.9	0.9	5.3	0.8	57.4	5.8
3.6.2015	15-5316	23.7	0.7	4.2	0.6	58.2	7.9
3.6.2015	15-5319	23.1	0.7	4.2	0.7	57.9	13.5

Table A.3: *Chemical analysis of the condensed water after air cleaning station (mg/kg).*

Date	Sample nr	CO_2	H_2S
8.7.2014	14-5216	5139.3	2445.5
11.7.2014	14-5217	4360.5	2285.8
25.9.2014	14-5333	4698.6	2521.7
16.10.2014	14-5363	4437.1	2567.8
21.10.2014	14-5370	4134.8	2397.5
4.12.2014	14-5414	4240.6	2494.6
19.12.2014	14-5453	4310.3	2669.7
16.1.2015	15-5033	4161.6	2821.4
18.3.2015	15-5206	3575.8	2434.8
13.4.2015	15-5243	4495.7	1891.5
15.4.2015	15-5247	4504.5	2604.6
13.5.2015	15-5263	4475.7	2565.8
1.6.2015	15-5283	4763.7	2311.7
1.6.2015	15-5286	4702.9	2118.6
1.6.2015	15-5289	4768.7	1945.4
2.6.2015	15-5292	4811.9	1823.1
2.6.2015	15-5294	4694.4	1727.4
2.6.2015	15-5296	4025.1	2471.9
2.6.2015	15-5298	3060.9	2176.8
2.6.2015	15-5300	1480.8	1107.3
2.6.2015	15-5302	987.0	761.8
2.6.2015	15-5304	867.4	668.0
3.6.2015	15-5307	5444.6	2694.6
3.6.2015	15-5309	5940.6	2699.9
3.6.2015	15-5311	2325.4	1770.6
3.6.2015	15-5313	2325.4	1770.6
3.6.2015	15-5315	2477.2	1746
3.6.2015	15-5317	2421.9	1886.5
3.6.2015	15-5320	2187.7	1792.2

B. Data Tables for Corrosion Rate

Table B.1: Corrosion rate measurements.

| Material | Identification and test nr [#] | Inital measurements (Average) | | | | | | Corrosion rate calculations | | |
		Coupon Weight [g]	Coupon Diameter [mm]	Coupon Thickness [mm]	Isolator Diameter [mm]	Weight Loss [g]	Density [g/m^3]	Surface area [cm^2]	Time [hours]	Corrosion rate [mm/yr]
S235 (St.37)	aa #1	33.89751	44.94	2.91	15.00	5.157957	7.85	32.30301	725.05	2.45754
S235 (St.37)	ab #1	31.50493	44.88	2.75	15.00	16.04612	7.85	31.98198	725.05	7.72202
S235 (St.37)	ac #1	32.95086	44.96	2.84	15.00	5.389745	7.85	32.23891	725.05	2.57309
S235 (St.37)	ad #1	32.21875	44.93	2.76	15.00	x	7.85	32.06625	725.05	x
S235 (St.37)	ae #2	27.58061	44.99	2.39	15.00	4.34213	7.85	31.64790	690.42	2.21758
S235 (St.37)	af #2	26.20153	45.00	2.33	15.00	14.82662	7.85	31.56805	690.42	7.59129
S235 (St.37)	ah #2	31.45161	45.01	2.75	15.00	5.1316	7.85	32.17735	690.42	2.57765
S235 (St.37)	ai #2	27.51888	44.96	2.41	15.00	x	7.85	31.61713	690.42	x
S235 (St.37)	aj #3	31.39054	44.98	2.74	15.00	5.556875	7.85	32.11821	2035.92	0.94832
S235 (St.37)	ak #3	34.03001	45.00	2.94	15.00	x	7.85	32.43066	2035.92	x
S235 (St.37)	al #3	32.55382	44.99	2.82	15.00	27.13483	7.85	32.25100	2035.92	4.61166
S235 (St.37)	am #3	32.15462	45.03	2.82	15.00	20.08799	7.85	32.29637	2035.92	3.40923
316L	ba #1	32.70128	44.78	2.82	15.00	-2.3E-05	7.8	31.93097	725.05	-0.00001
316L	bb #1	35.04660	44.97	2.99	15.00	x	7.8	32.45644	725.05	x
316L	bc #1	34.51997	44.71	2.96	15.00	-0.0007	7.8	32.01832	725.05	-0.00034
316L	bd #1	35.12863	44.73	3.02	15.00	-0.00069	7.8	32.13258	725.05	-0.00033
316L	be #2	30.62529	44.87	2.61	15.00	x	7.8	31.77493	690.42	x
316L	bf #2	30.13198	44.97	2.58	15.00	0.00045	7.8	31.88160	690.42	0.00023
316L	bh #2	30.21589	44.92	2.59	15.00	0.0004	7.8	31.81608	690.42	0.00020
316L	bi #2	27.92971	44.86	2.48	15.00	0.00041	7.8	31.57183	690.42	0.00021
316L	bj #3	31.02757	44.66	2.71	15.00	-0.00021	7.8	31.59303	2035.92	-0.00004
316L	bk #3	34.28179	45.02	2.93	15.00	6.5E-05	7.8	32.44162	2035.92	0.00001
316L	bl #3	30.11283	44.95	2.61	15.00	-0.00016	7.8	31.88911	2035.92	-0.00003
316L	bm #3	33.58566	44.63	2.94	15.00	x	7.8	31.87089	2035.92	x
2205	ca #1	30.97938	44.90	2.70	15.00	0.001572	7.8	31.93697	725.05	0.00076
2205	cb #1	28.01341	44.99	2.46	15.00	-0.00202	7.8	31.73246	725.05	-0.00098
2205	cc #1	30.85155	44.95	2.66	15.00	x	7.8	31.95972	725.05	x
2205	cd #1	30.75182	44.98	2.71	15.00	-0.00045	7.8	32.07554	725.05	-0.00022
2205	ce #2	29.64252	44.91	2.65	15.00	-0.00028	7.8	31.89079	690.42	-0.00014
2205	cf #2	32.37570	44.97	2.85	15.00	x	7.8	32.25834	690.42	x
2205	ch #2	25.31705	44.90	2.28	15.00	0.00134	7.8	31.35887	690.42	0.00070
2205	ci #2	27.43924	44.95	2.41	15.00	0.00073	7.8	31.59729	690.42	0.00038
2205	cj #3	32.97550	45.01	2.86	15.00	x	7.8	32.33731	2035.92	x
2205	ck #3	31.01257	44.99	2.71	15.00	0.00162	7.8	32.08552	2035.92	0.00028
2205	cl #3	30.65125	44.97	2.71	15.00	-0.00142	7.8	32.06084	2035.92	-0.00024
2205	cm #3	32.26277	44.97	2.81	15.00	-0.00294	7.8	32.21155	2035.92	-0.00050

B. Data Tables for Corrosion Rate

Table B.2: Corrosion rate results for Carbon steel Test 1. S235 carbon steel coupons.

	Inital measurements (Average)				Corrosion rate calculations				
Identification	Coupon Weight	Coupon Diameter	Coupon Thickness	Isolator Diameter	Weight Loss	Density	Surface area	Time	Corrosion rate
	[g]	[mm]	[mm]	[mm]	[g]	[g/m^3]	[cm^2]	[hours]	[mm/yr]
A	34.08517	44.90	2.94	15	3.940487	7.85	32.28491	432.5	3.149188
B	33.90491	44.85	2.94	15	3.38946	7.85	32.20541	432.5	2.715501
C	34.08966	44.91	2.94	15	6.289287	7.85	32.29493	432.5	5.02476
F	34.38658	44.93	2.95	15	8.53431	7.85	32.34915	432.5	6.806971
G	34.24686	44.92	2.95	15	8.195333	7.85	32.33410	432.5	6.539644
H	34.45498	44.93	2.97	15	7.482693	7.85	32.37267	432.5	5.963864
I	34.46614	44.92	2.97	15	7.203853	7.85	32.34791	432.5	5.746018
L	34.20557	44.92	2.95	15	6.49710	7.85	32.32909	432.5	5.185306
M	34.39277	44.92	2.97	15	6.12874	7.85	32.35763	432.5	4.887006
N	34.45137	44.95	2.96	15	5.628947	7.85	32.37862	432.5	4.485565
R	34.38609	44.89	2.97	15	5.56367	7.85	32.3078	432.5	4.443266
S	34.4394	44.94	2.96	15	5.71369	7.85	32.36828	432.5	4.554549

Table B.3: Corrosion rate results for Carbon steel Test 2. S235 carbon steel coupons.

|	Inital measurements (Average)				Corrosion rate calculations				
Identification	Coupon Weight	Coupon Diameter	Coupon Thickness	Isolator Diameter	Weight Loss	Density	Surface area	Time	Corrosion rate
	[g]	[mm]	[mm]	[mm]	[g]	[g/m^3]	[cm^2]	[hours]	[mm/yr]
A	30.14468	44.74	2.84	15	1.99491	7.85	31.89959	408	1.71046
B	30.51545	44.28	2.73	15	3.09115	7.85	31.06230	408	2.72183
C	27.80037	44.31	2.41	15	4.56138	7.85	30.66116	408	4.06895
F	25.85227	44.51	2.52	15	2.61328	7.85	31.10916	408	2.29759
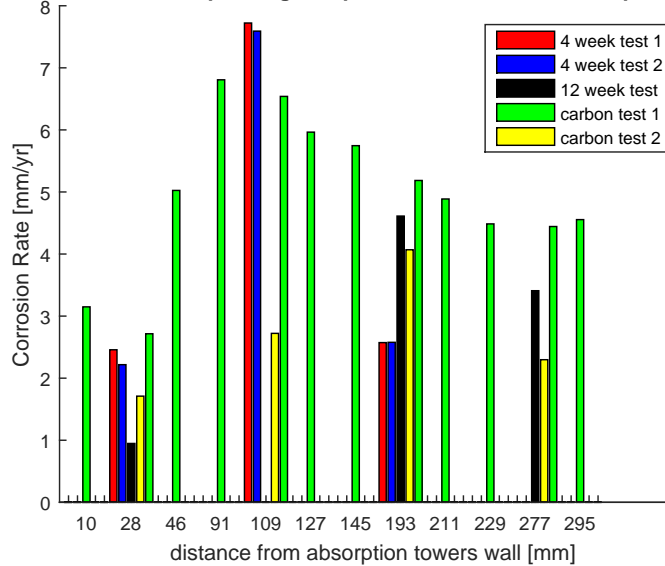
Figure B.1: Comparison graph of the corrosion rate for all the experiments
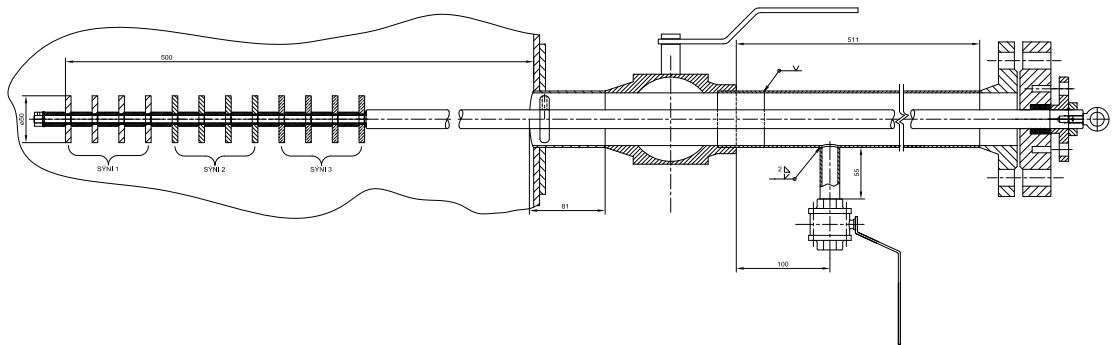
C. Schematic Design of the Specimen Holder

Figure C.1: Schematic design of specimen holder